Autonomous Heavy Object Pushing Using a Coaxial Tiltrotor

Sunwoo Hwang*, Dongjae Lee*, Changhyeon Kim, and H. Jin Kim

***Abstract*—Aerial physical interaction (APhI) with a multirotor-based platform such as pushing a *heavy* object demands generation of a sufficiently large interaction force while maintaining the stability. Such requirement can cause rotor saturation, because the rotor thrust enlarged for interaction force may leave a reduced margin for attitude stabilization. We first design an H-shaped coaxial tiltrotor that can generate a sufficiently large interaction force than a conventional multirotor. We then propose an overall framework composed of high-level robust controller and low-level control allocation for the coaxial tiltrotor to ensure robustness against uncertain motion of the unknown interacting object and to overcome the saturation issue. To guarantee the robustness at all time, we design a controller based on a nonlinear disturbance observer (DOB). Then, we formulate a problem of computing low-level actuator inputs avoiding rotor saturation as a tractable nonlinear optimization problem, which can be solved real-time. The proposed framework is validated in extensive real-world experiments where the 3.3 kg tiltrotor successfully pushes a cart weighing up to 60 kg. An ablation study with the tiltrotor shows effectiveness of the proposed control allocation law in avoiding rotor saturation. Furthermore, a comparative experiment with a conventional multirotor shows failure in the same setting, which validates the use of the coaxial tiltrotor. An experimental video can be found at https://youtu.be/Gdmcmoz_UjU**

***Note to Practitioners*—The motivation of this work is to enable heavy object manipulation, especially pushing operation, using a multirotor platform. To push a heavy object, which has not been treated in existing works, is challenging due to the presence of a large unknown interaction wrench and rotor saturation issue. To resolve this problem, we first build an H-shaped coaxial tiltrotor that can effectively utilize rotor thrusts to generate horizontal interaction force. Then, a robust controller is designed to address uncertainty in the interaction wrench for the tiltrotor. Finally, we propose an optimization-based control allocation to avoid rotor saturation. Real-world experiments including heavy object pushing and ablation study with respect to the control allocation law are conducted to show the effectiveness of the proposed framework. We validate the use of the coaxial tiltrotor in additional comparative experiments with a conventional multirotor which fails in pushing a 60 kg cart. The proposed framework can be utilized in various applications such as disaster relief operations, emergency rescue and aerial delivery.**

***Index Terms*—robust control, disturbance observer, control allocation, rotor saturation, tiltrotor, aerial physical interaction**

*The first two authors contributed equally to this work.

This work was supported by Unmanned Vehicles Core Technology Research and Development Program through the National Research Foundation of Korea(NRF) and Unmanned Vehicle Advanced Research Center(UVARC) funded by the Ministry of Science and ICT(NRF-2020M3C1C1A010864).

S. Hwang, D. Lee and H. Jin Kim are with the Department of Aerospace Engineering and the Automation and Systems Research Institute (ASRI), Seoul National University, Seoul 08826, South Korea {swsw0411,ehdwo713,hjinkim}@snu.ac.kr

C. Kim is with Robot Intelligence Team, Samsung Research, Seoul 06772, South Korea ch_.kim@samsung.com

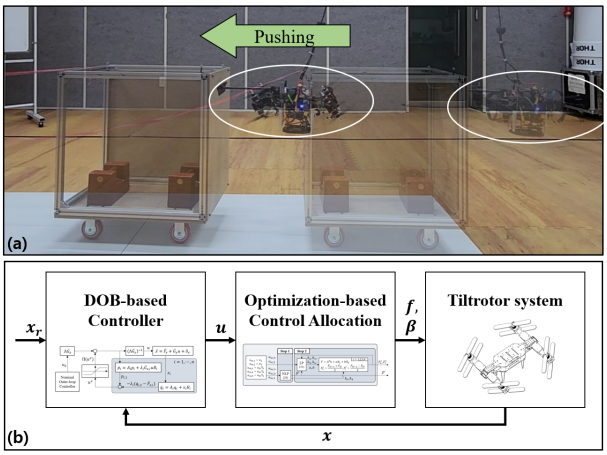

Fig. 1. (a) The 3.3 kg tiltrotor is pushing a 60 kg cart without losing stability. (b) Overall control framework including controller and control allocation. x^r and x are reference trajectory and state feedback, respectively. u is a high-level input computed by controller where F, β^c denote a low-level actuator input consisting of thrust F and servomotor command β^c.

I. INTRODUCTION

Aerial robots have potential to conduct aerial physical interactions (APhI) with a dynamic environment in various situations such as disaster relief operation, emergency rescue, and aerial delivery. To further enhance utility and efficiency of a single aerial robot in APhI tasks beyond those demonstrated in literature, such as opening a door [1], [2] or pushing a cart [3], [4], the aerial robot should be capable of manipulating objects much heavier than the robot itself.

Since the manipulation of heavy objects using an aerial robot requires both a sufficiently large interaction wrench for manipulation and a gravity-compensating force for hovering, input saturation should be carefully addressed. If not tackled properly, the saturation in the control input can cause not only the degradation in the control performance but also the loss of stability [5]. In addition, several issues including unexpected motion of an environment and unknown time-varying interaction wrench should be carefully managed for successful heavy object manipulation using an aerial robot.

As one representative task of heavy object manipulation, this work focuses on pushing. To resolve the problems of 1) uncertainty in the motion of an interacting object and interaction wrench and 2) input saturation, this work presents an overall framework consisting of a robust controller design and control allocation for an H-shaped coaxial tiltrotor. The coaxial tiltrotor in Fig. 1 is designed for its capability of generating a sufficiently large interaction wrench compared

to the tiltrotor's weight. Then, to endow robustness during interaction with a dynamic object, we construct a robust controller applicable to the tiltrotor. We enhance flexibility in the gain tuning process by introducing a multivariable control gain responsible for rejecting disturbance instead of a scalar control gain adopted in existing works [6]–[8]. This modification allows users to separately tune control gains in all 6-dimensional translational and rotational directions. Finally, we formulate a control allocation algorithm as a hierarchical optimization problem to avoid rotor saturation while ensuring real-time applicability (> 200 Hz). The overall framework is demonstrated in real-world experiments where extensive results validate the proposed framework in heavy object pushing where the 3.3 kg coaxial tiltrotor successfully pushes an approximately 20 times heavier 60 kg cart as in Fig. 1.

A. Related Works

1) Robust Controller Design for APhI: Various APhI papers employ robust control [7]–[10] to treat the interaction wrench as a disturbance to be compensated. Especially during APhI with a dynamic environment, both steady-state and transient performances are critical because the interaction force is correlated to the relative motion between the multirotor and the interacting object. The robust controller in [10] for the tiltrotor can provide guarantee in the steady-state performance only, not transient performance. [11] presents a robust model reference adaptive control for a tiltrotor that guarantees both performances, but the controller requires the upper bound of external disturbance, which may limit practicality. Robust controllers based on a nonlinear disturbance observer (DOB) [7], [8] or a prescribed performance control [9] are proposed for a convevntional multirotor to ensure both performances, which alleviate the need for the upper bound of external disturbance. For the tiltrotor platform, however, a new controller needs to be constructed due to its additional control degrees of freedom (CDoF).

In designing DOB, a control gain responsible for rejecting disturbance is originally defined to be a single scalar [6]–[8]. However, referring to equations of motion of a rigid body, dynamic characteristics of 6-dimensional translation and rotation are dissimilar. Therefore, tuning a proper scalar gain appropriate for each state channel can be demanding in practice.

2) Control Allocation for Multirotors: In solving a control allocation problem for the designed coaxial tiltrotor, hardware-inherent nonlinearity and redundancy caused by the tilting mechanism and overactuation should be suitably addressed. Thus, we review papers on similar control allocation problems for multirotor platforms. First regarding hardware-inherent nonlinearity, [12]–[14] adopt a variable transformation method for a fully actuated tiltrotor. Similarly, the method is applied to 5-CDoF tiltrotors in [11], [15], [16]. However, such method assumes that the tilt angle of individual rotors (or rotor groups if they are coaxial) can be independently controlled, which is not applicable to our platform. Instead of regarding tilt angles of rotors as a control input, [14], [17] utilize angular velocity of the tilt angles and bypass nonlinearity. However, since they require acceleration measurement which is susceptible to sensor noise in practice, control performance may easily get deteriorated.

Next, in handling redundancy, the Moore-Penrose pseudo-inverse of a matrix can be applied [18], [19]. For the H-shaped tiltrotor, [10] suggests an optimization problem minimizing overall thrust where redundancy is resolved. To further exploit redundancy, one popular approach is to deploy null-space in achieving secondary objectives [14], [17], [20], [21]. They utilize null-space to handle singularity [17], [20], to avoid downwash effect [21] or to achieve cable unwinding [14]. However, rotor saturation avoidance is not considered in the aforementioned works. [22] presents a QP formulation to handle rotor saturation partially in solving the control allocation problem, but not the rotor saturation avoidance which is to minimize maximum rotor thrust among 16 rotors of an over-actuated multirotor. Although [23] considers rotor dynamics and rotor saturation in solving a control allocation problem, its method is only applicable to an underactuated multirotor which does not involve hardware-inherent nonlinearity. To the best of the authors' knowledge, no work on tiltrotors considers minimizing the maximal rotor thrust over all rotors to avoid saturation in harnessing redundancy.

B. Contribution

The proposed framework includes the following contributions:

- We propose a nonlinear DOB-based robust controller for a 5-CDoF underactuated tiltrotor which theoretically guarantees both transient and steady-state performances during object pushing. Furthermore, to facilitate gain tuning in each translational and rotational direction, we introduce a multivariable control gain responsible for compensating disturbance, unlike existing works [6]–[8] that use a scalar control gain.
- We propose a hierarchical optimization-based control allocation law for rotor saturation avoidance, energy consumption reduction, and servomotors' position error minimization with real-time applicability. To the best of the authors' knowledge, the control allocation method to avoid rotor saturation is suggested for the first time for a tiltrotor.
- We conduct real-world experiments of pushing a cart up to 60 kg which is roughly 20 times heavier than the 3.3 kg tiltrotor. Furthermore, a comparative study with a conventional multirotor validates the effectiveness of the proposed framework using a coaxial tiltrotor.

C. Preliminary Notations

In this study, $c*$, $s*$, and $t*$ denote shorthands for $\cos(*)$, $\sin(*)$, and $\tan(*)$, respectively. For convenience, we use $[a; b]$ to express $[a^\top \ b^\top]^\top$. Furthermore, x_i and M_i denote i^{th} element of the vector $\boldsymbol{x}$ and i^{th} row of the matrix M. For clear distinguishment, we use lowercase letters for scalars, bold lowercase letters for vectors, and uppercase letters for matrices. For unit vectors, we define $\boldsymbol{e_1} = [1; 0; 0]$, $\boldsymbol{e_2} = [0; 1; 0]$, and

$\boldsymbol{e_3} = [0; 0; 1]$. I_n and $0_{j\times k}$ denote an identity matrix in $\mathbb{R}^{n\times n}$ and a zero matrix in $\mathbb{R}^{j\times k}$. $(\hat{\cdot})$ operator is a mapping from $\mathbb{R}^3$ to $so(3)$. Finally, we define $E_5 \in \mathbb{R}^{6\times 5}$ eliminating the second row of an operand as $E_5 = \texttt{blockdiag}\{[1; 0], I_4\}$.

II. HARDWARE CONSIDERATION

During APhI, external torque disturbance is inevitable due to tangential friction between an environment and an end-effector of a multirotor-based aerial manipulator. Moreover, in most APhI tasks, simultaneously achieving gravity compensation and sufficient interaction force generation is essential. As a result, the average rotor thrust exceeds the hovering threshold, which reduces the margin available for rotor thrust. Meanwhile, conventional multirotor generates yaw directional body torque solely relying on aerodynamic drag. Here, a drag coefficient k_f which denotes the thrust-torque ratio is generally small as 10^{-2} scale. Therefore, to perform APhI with a conventional multirotor, a large difference in the rotor thrusts should be generated despite the lowered thrust margin, and thus, rotor saturation is highly likely.

To overcome this issue, we seek a new multirotor platform that can harness rotor thrust as an additional source in generating yaw torque during APhI. Such actuation property can be achieved either by disposing rotors with fixed tilt angle [19], [24], [25] or enabling thrust vectoring [10]–[13], [15]–[17], [26]–[31]. Since both methods can generate horizontal body force using rotors with nonzero tilt angle, yaw torque can be induced accordingly.

To ensure a sufficiently large interaction force margin, we mainly consider and devise the following three criteria:

C1) The ratio of available thrust to the weight of the platform should be sufficiently large.
C2) Thrust cancellation among rotors should not exist in any direction.
C3) All rotors should contribute to horizontal force generation during APhI.

To design a platform that fulfills the three criteria, we adopt an H-shaped coaxial tiltrotor (see Fig. 2). First, the platform utilizes only two servomotors to achieve thrust vectoring [10], [29], thus the weight of added apparatus for thrust vectoring can be kept small. Second, since the rotating axes of the servomotors are parallel, thrust cancellation can be avoided. Lastly, because all rotors can be rotated in the same direction, all rotors can contribute to horizontal force generation during APhI.

The H-shaped tiltrotor has advantages in the perspective of the criterion C2 compared to the aerial platforms used in [19], [24], [25]. This is because a fixed tilt angle configuration utilized in these works causes inevitable thrust cancellation during flight. The most widely adopted method to obtain thrust vectoring capability is to deploy additional servomotors, which is also used in the designed H-shaped tiltrotor. In [11], [13], [15], [17], [26], [27], they assign one servomotor per each rotor (or rotor group if coaxial). Although such approach enables to control the full pose of an aerial robot [13], [17], [27] or achieves high maneuverability [15], most of the approaches suffer from thrust cancellation (violation of C2),

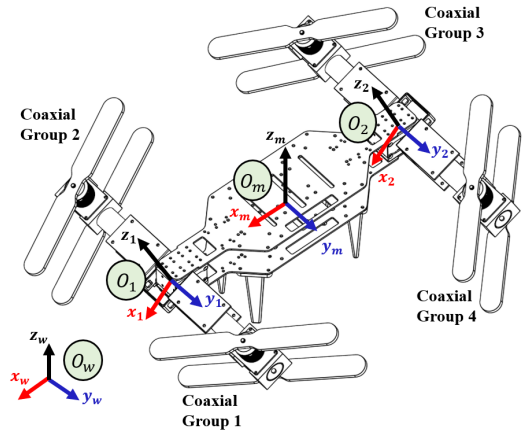

(a) Tiltrotor

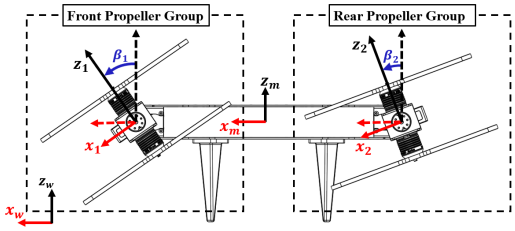

(b) Sideview

Fig. 2. Illustration of the redesigned 5-CDoF tiltrotor. (a) O_1, O_m, O_2 denote moving coordinate frames of rigid bodies where O_w denotes the world inertial frame. The index of each coaxial rotor group is introduced. (b) Tilt angles β_1, β_2 of front and rear propeller groups are shown.

and the use of excessively many servomotors (4 or 6) may lead to an unnecessary increase of the dead weight of an aerial robot (violation of C1). [16], [28], [30] utilize fewer servomotors, or even no servomotor just by relying on a passive mechanism [31], but such configuration may limit the use of all rotors in horizontal force generation during APhI, violating the criterion C3. There exist other aerial platforms [12], [21], [32] capable of thrust vectoring by which rotor thrust can participate in yaw torque generation. However, unlike the H-shaped tiltrotor used in this work, not all three criteria can be satisfied with those platforms.

III. DYNAMICS

The tiltrotor used in this work consists of three rigid bodies: front propeller group including coaxial groups 1 and 2, main body, and rear propeller groups including coaxial groups 3 and 4 (see Fig. 2). Coordinate frames with the origin located at the geometric center of each rigid body are defined as illustrated in Fig. 2 where O_w is the world inertial frame.

In deriving dynamics of the tiltrotor, m_b and J_b denote the mass and inertia matrix of the main body (O_m). Also, m_p and J_p are the mass and inertia matrix of each propeller group (O_1, O_2), and $m = m_b + 2m_p$ indicates the total mass of the tiltrotor. We define ${}^iR_j \in SO(3)$ as the orientation of the frame O_j written in the frame O_i for $i, j \in \{1, 2, m, w\}$ and $R = {}^wR_m$ for simplicity. Finally, for $i = m, 1, 2$, $\boldsymbol{x_i}$ denotes the position of O_i written in O_w, and $\boldsymbol{\omega_i}$ denotes the angular velocity of O_i written in O_i.

A. Actual Dynamic Model

We select a generalized coordinate $\boldsymbol{\chi_g} = [\boldsymbol{\chi}; \boldsymbol{\beta}] \in \mathbb{R}^8$ where $\boldsymbol{\chi} = [\boldsymbol{x_m}; \boldsymbol{\phi}] \in \mathbb{R}^6$ consists of the position $\boldsymbol{x_m} = [x; y; z]$ and ZYX Euler angles $\boldsymbol{\phi_m} = [\phi; \theta; \psi]$ of O_m, and $\boldsymbol{\beta} = [\beta_1; \beta_2]$ denotes a vector of rotation angles of O_1, O_2 in their body y-axis, respectively (Fig. 2).

Exploiting the Euler-Lagrange equation [33], the equation of motion is derived as

$$M_g \ddot{\boldsymbol{\chi}}_{\boldsymbol{g}} + C_g \dot{\boldsymbol{\chi}}_{\boldsymbol{g}} + \boldsymbol{k_g} = \boldsymbol{\tau_g} + \boldsymbol{\tau_{g,ext}} \tag{1}$$

where M_g, $C_g \in \mathbb{R}^{8\times 8}$ and $\boldsymbol{k_g} \in \mathbb{R}^8$ are the mass and Coriolis-centrifugal matrices and gravitational vector, and $\boldsymbol{\tau_g}$, $\boldsymbol{\tau_{g,ext}} \in \mathbb{R}^8$ are generalized torque and external disturbance. $\boldsymbol{\tau_{g,ext}}$ can include any additive disturbance such as the near-wall effect and an interaction wrench during APhI. Now, extracting first six rows of the equation (1), the dynamics of $\boldsymbol{\chi}$ can be obtained as follows:

$$M\ddot{\boldsymbol{\chi}} + C\dot{\boldsymbol{\chi}} + \boldsymbol{k} = \hat{Q}^\top \boldsymbol{\tau} + \boldsymbol{\Delta} \tag{2}$$

where

$$\boldsymbol{\Delta} = \boldsymbol{\tau_{ext}} - \begin{bmatrix} 0_{3\times 1} \\ J_p(2,2) Q^\top \boldsymbol{e_2} \end{bmatrix} (\ddot{\beta}_1 + \ddot{\beta}_2) - \begin{bmatrix} 0_{3\times 2} \\ C_{23} \end{bmatrix} \dot{\boldsymbol{\beta}},$$

and $M = \hat{Q}^\top M_b \hat{Q}$, $\hat{Q} = \texttt{blockdiag}\{R^\top, Q\}$,

$$M_b = \begin{bmatrix} mI_3 & 0_{3\times 3} \\ 0_{3\times 3} & J_b + 2m_p l_2^2 \hat{\boldsymbol{e}}_{\boldsymbol{1}}^\top \hat{\boldsymbol{e}}_{\boldsymbol{1}} + \sum_{i=1}^{2} {}^bR_i J_p {}^bR_i^\top \end{bmatrix}.$$

$C_{23} \in \mathbb{R}^{3\times 2}$ is a coupling term between $\boldsymbol{\phi}_m$ and $\boldsymbol{\beta}$ extracted from C_g. Also, l_2 denotes half of the distance between front and rear propeller groups, and Q is the Jacobian matrix satisfying $\boldsymbol{\omega_m} = Q\dot{\boldsymbol{\phi}}_{\boldsymbol{m}}$. Moreover, $\boldsymbol{\tau} = [\boldsymbol{f_b}; \boldsymbol{\tau_b}] \in \mathbb{R}^6$ denotes generated body force/torque written in O_m. We lump all the remaining terms in the right-hand side of (2) as $\boldsymbol{\Delta}$ which is considered as disturbance. Compared to the fact that a conventional multirotor has 4-CDoF, the tiltrotor has 5-CDoF thanks to the tilting mechanism. Thus, we can define a control input $\boldsymbol{u} \in \mathbb{R}^5$ satisfying $\boldsymbol{\tau} = E_5 \boldsymbol{u}$ where $\boldsymbol{u}$ consists of forces in body x and z axes $f_{b,1}$, $f_{b,3}$, and a body torque $\boldsymbol{\tau_b} \in \mathbb{R}^3$.

Now, for the ease of controller design of the 5-CDoF tiltrotor, we divide the entire system into fully actuated and underactuated subsystems whose configurations are defined as $\boldsymbol{x_f} = [x; z; \phi; \theta; \psi] \in \mathbb{R}^5$ and $x_u = y \in \mathbb{R}$, respectively. We can obtain 5-dimensional dynamics of the fully actuated subsystem by pre-multiplying $E_5^\top M^{-1}$ to (2) as

$$\ddot{\boldsymbol{x}}_{\boldsymbol{f}} = \boldsymbol{f_f} + G_f \boldsymbol{u} + \boldsymbol{\Delta_f} \tag{3}$$

where $\boldsymbol{f_f} = -E_5^\top M^{-1}(C\dot{\boldsymbol{\chi}} + \boldsymbol{k})$, $G_f = E_5^\top M^{-1} \hat{Q}^\top E_5$, and $\boldsymbol{\Delta_f} = E_5^\top M^{-1} \boldsymbol{\Delta}$. Moreover, the underactuated subsystem can be derived from the second row of (2) as

$$\ddot{x}_u = f_u + G_u \tan\phi^r + \Delta_u \tag{4}$$

where $f_u = u_1 c\theta s\psi/m + u_2 c\phi s\theta s\psi/m$, $G_u = -u_2 c\phi c\psi/m$, and Δ_u contains external disturbance in global y direction and matched disturbance $G_u(t\phi - t\phi^r)$. Here, ϕ^r denotes a reference value of ϕ where $\tan\phi^r$ is a virtual control input to the underactuated subsystem.

B. Nominal Dynamic Model

We derive the nominal dynamics of the system with the Newton-Euler equation. Considering the tiltrotor as a single rigid body by assuming a constant inertia matrix with $\boldsymbol{\beta} = 0_{2\times 1}$, we can use the following 3-dimensional rigid body dynamics:

$$m\ddot{\boldsymbol{x}}_{\boldsymbol{m}} = -mg\boldsymbol{e_3} + R\boldsymbol{f_b}$$
$$J\dot{\boldsymbol{\omega}}_{\boldsymbol{m}} = -\hat{\boldsymbol{\omega}}_{\boldsymbol{m}} J \boldsymbol{\omega_m} + \boldsymbol{\tau_b}$$

where $J = J_b + 2m_p l_2^2 \hat{\boldsymbol{e}}_{\boldsymbol{1}}^\top \hat{\boldsymbol{e}}_{\boldsymbol{1}} + 2J_p$ denotes the nominal inertia matrix of the tiltrotor. Using the fact that $[\boldsymbol{f_b}; \boldsymbol{\tau_b}] = E_5 \boldsymbol{u}$, the nominal dynamics of (3) can be written as

$$\ddot{\boldsymbol{x}}_{\boldsymbol{f}} = \bar{\boldsymbol{f}}_{\boldsymbol{f}} + \bar{G}_f \bar{\boldsymbol{u}} \tag{5}$$

where $\bar{\boldsymbol{f}}_{\boldsymbol{f}} = [0; -g; -Q^{-1}(\dot{Q}\dot{\boldsymbol{\phi}}_{\boldsymbol{m}} + J^{-1}\hat{\boldsymbol{\omega}}_{\boldsymbol{m}} J \boldsymbol{\omega_m})]$, $\bar{G}_f = E_5^\top \hat{Q}^{-1} \bar{M}_b^{-1} E_5$, $\bar{M}_b = \texttt{blockdiag}\{mI_3, J\}$ and $\bar{\boldsymbol{u}}$ denotes the nominal control input. Likewise, the nominal dynamics of (4) can be written as

$$\ddot{x}_u = \bar{f}_u + \bar{G}_u \tan\bar{\phi}^r \tag{6}$$

where $\bar{f}_u$, $\bar{G}_u$ denote the nominal value of f_u, G_u computed by replacing $\boldsymbol{u}$ with $\bar{\boldsymbol{u}}$, respectively, and $\bar{\phi}^r$ is the nominal signal of ϕ^r.

IV. CONTROLLER DESIGN

For pushing a heavy object, a sufficiently large interaction force is required to manipulate an object with unknown inertia and friction. However, since the required magnitude of the interaction force is unknown, the object can only be moved by gradually increasing the interaction force. For this purpose, we adopt a robust controller to generate increasing interaction force until the object starts to move. However, if steady-state performance is only guaranteed as in [10], a transient performance due to time-varying interaction force can be degraded. To handle this issue, we design a robust controller for the coaxial tiltrotor based on nonlinear DOB [34] which guarantees both transient and steady-state performances.

A. DOB Formulation

In this subsection, we consider n-dimensional general control-affine nonlinear system and analyze the stability of the system with the proposed DOB-based control law. We first define actual and nominal systems as follows:

$$\ddot{\boldsymbol{x}} = \boldsymbol{f_x} + G_x \boldsymbol{u} + \boldsymbol{\Delta_x} \tag{7}$$
$$\ddot{\bar{\boldsymbol{x}}} = \bar{\boldsymbol{f}}_{\boldsymbol{x}} + \bar{G}_x \bar{\boldsymbol{u}} \tag{8}$$

where $\boldsymbol{x}$, $\bar{\boldsymbol{x}}$, $\boldsymbol{u}$, $\boldsymbol{f_x}$, $\bar{\boldsymbol{f}}_{\boldsymbol{x}}$, $\boldsymbol{\Delta_x} \in \mathbb{R}^n$ and G_x, $\bar{G}_x \in \mathbb{R}^{n\times n}$. Here, we allow a slight abuse of notation for indicating the system state and input as $[\boldsymbol{x}; \dot{\boldsymbol{x}}]$ and $\boldsymbol{u}$, respectively. To conduct a simpler analysis, we rewrite (7) as

$$\begin{aligned} \ddot{\boldsymbol{x}} &= \bar{\boldsymbol{f}}_{\boldsymbol{x}} + \bar{G}_x \boldsymbol{u} + [\boldsymbol{\Delta_x} + (\boldsymbol{f_x} - \bar{\boldsymbol{f}}_{\boldsymbol{x}}) + (G_x - \bar{G}_x)\boldsymbol{u}] \\ &= \bar{\boldsymbol{f}}_{\boldsymbol{x}} + \bar{G}_x \boldsymbol{u} + \boldsymbol{\delta_x} \end{aligned} \tag{9}$$

where $\boldsymbol{\delta_x} \in \mathbb{R}^n$ can be treated as lumped disturbance. Moreover, there may exist an underactuated subsystem that can be controlled by $\boldsymbol{x}$, $\dot{\boldsymbol{x}}$. We express such underactuated

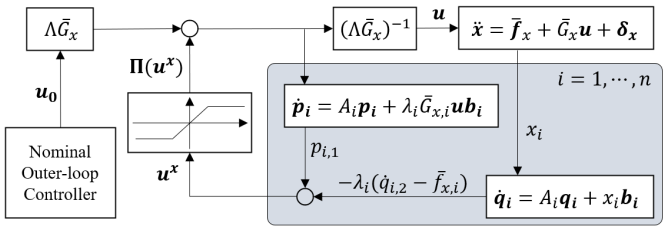

Fig. 3. Proposed inner-loop controller (10). Compared to previous nonlinear DOBs [6], [7], we allow to use of different ϵ_i for each x_i. This allows additional freedom in the gain tuning process while preserving desirable stability properties. Signal flows of inner-loop vectors u^x, q, p are shown.

subsystem as $\ddot{\boldsymbol{y}} = \boldsymbol{f_y} + G_y\boldsymbol{v_y}(\boldsymbol{x}, \dot{\boldsymbol{x}})$ where $[\boldsymbol{y}; \dot{\boldsymbol{y}}]$ is the underactuated state and $\boldsymbol{v_y}(x, \dot{x})$ denotes a function of the system state which can be manipulated as a virtual control input.

In the following, we first present a definition of sets and a few assumptions to formally derive the proposed DOB formulation.

Definition 1. *First, define $\mathcal{U}_x$ as a known bounded set of $[\boldsymbol{x}; \dot{\boldsymbol{x}}]$. Then, we define $\mathcal{S}_x \subset \mathcal{U}_x$ as a compact set and $\bar{\mathcal{S}}_x$ as a slightly smaller compact subset of $\mathcal{S}_x$. If there exists an underactuated subsystem described with a configuration $\boldsymbol{y}$, sets $\mathcal{U}_y$, $\mathcal{S}_y$ and $\bar{\mathcal{S}}_y$ are defined in the same manner.*

Assumption 1. *If there exists an underactuated subsystem initialized with $[\boldsymbol{y}(0); \dot{\boldsymbol{y}}(0)] \in \mathcal{S}_y$ and controlled by $[\boldsymbol{x}; \dot{\boldsymbol{x}}] \in \mathcal{U}_x$, then $[\boldsymbol{y}(t); \dot{\boldsymbol{y}}(t)] \in \mathcal{U}_y$ is satisfied.*

Assumption 2. *$\bar{\boldsymbol{f}}_{\boldsymbol{x}}$, $\bar{G}_x$, $\bar{G}_x^{-1}$ and $\boldsymbol{\delta_x}$ are at least $\mathcal{C}^1$ and bounded in $\mathcal{U}_x \times \mathcal{U}_y$.*

Informally speaking, the assumptions are nothing but 1) boundedness of the underactuated subsystem and 2) differentiability of the external disturbance $\boldsymbol{\Delta_x}$. Note that these assumptions are widely adopted and easily satisfied in various robust control applications, for example, by adopting PD control for the virtual control input and considering aerodynamic effect and model uncertainty for disturbance. Thus, these assumptions do not strongly restrict the applicability of the proposed controller.

Now, we present the proposed DOB structure to design a controller that guarantees both steady-state and transient performances. As illustrated in Fig. 3, the proposed DOB consists of inner-loop vectors $\boldsymbol{u^x} \in \mathbb{R}^n$, $\boldsymbol{q} = [\boldsymbol{q_1}; \boldsymbol{q_2}; ...; \boldsymbol{q_n}]$, $\boldsymbol{p} = [\boldsymbol{p_1}; \boldsymbol{p_2}; ...; \boldsymbol{p_n}] \in \mathbb{R}^{2n}$ where $\boldsymbol{q_i} = [q_{i,1}; q_{i,2}]$, $\boldsymbol{p_i} = [p_{i,1}; p_{i,2}] \in \mathbb{R}^2$ for $i = 1, 2, ..., n$. The above variables are updated as

$$\begin{aligned} &\dot{\boldsymbol{q}}_{\boldsymbol{i}} = A_i\boldsymbol{q_i} + x_i\boldsymbol{b_i}, \quad \dot{\boldsymbol{p}}_{\boldsymbol{i}} = A_i\boldsymbol{p_i} + \lambda_i\bar{G}_{x,i}\boldsymbol{u}\boldsymbol{b_i}, \\ &u_i^x = p_{i,1} - \lambda_i(\dot{q}_{i,2} - \bar{f}_{x,i}), \\ &\boldsymbol{u} = \boldsymbol{u_0} + (\Lambda\bar{G}_x)^{-1}\boldsymbol{\Pi}(\boldsymbol{u^x}) \end{aligned} \tag{10}$$

where

$$\begin{aligned} A_i &= \begin{bmatrix} 0 & 1 \\ -a_{i,0}/\epsilon_i^2 & -a_{i,1}/\epsilon_i \end{bmatrix}, \quad \boldsymbol{b_i} = \begin{bmatrix} 0 \\ a_{i,0}/\epsilon_i^2 \end{bmatrix}, \\ \Lambda &= \mathtt{diag}(\lambda_1, \lambda_2, ..., \lambda_n) \in \mathbb{R}^{n\times n}, \\ E &= \mathtt{diag}(\epsilon_1, \epsilon_2, ..., \epsilon_n) = \epsilon_x S \in \mathbb{R}^{n\times n}, \end{aligned}$$

and $\boldsymbol{u_0}$ is any $\boldsymbol{u_0} \in \mathcal{C}^1$ outer-loop control law that drives the nominal system (8) with $\bar{\boldsymbol{u}} = \boldsymbol{u_0}$ asymptotically stable. Here, $a_{i,0}$, $a_{i,1}$, $\lambda_i \in \mathbb{R}_{++}$ are design parameters and $\epsilon_i \in \mathbb{R}_{++}$ is sufficiently small value. Note that unlike previous works [6]–[8], we allow different ϵ_i's along each state channel x_i which facilitates gain tuning process. To denote that all the diagonal elements of E satisfy $\epsilon_i \in O(\epsilon_x)$ for an arbitrarily small scalar ϵ_x, we introduce a constant diagonal matrix S. This condition is imposed to preserve the stability property while allowing different ϵ_i's. Moreover, $\Pi(\cdot) : \mathbb{R}^n \to \mathbb{R}^n$ is the globally bounded $\mathcal{C}^1$ saturation function which satisfies

$$\begin{aligned} \boldsymbol{\Pi}(\boldsymbol{u^x}) &= \boldsymbol{u^x} \quad \forall \boldsymbol{u^x} \in \mathcal{S}_{u^x}, \\ \|\partial\boldsymbol{\Pi}(\boldsymbol{u^x})/\partial\boldsymbol{u^x}\| &\le 1 \quad \forall \boldsymbol{u^x} \in \mathbb{R}^n \end{aligned}$$

where $\mathcal{S}_{u^x}$ denotes the steady-state range of u^x defined as

$$\mathcal{S}_{u^x} = \{\boldsymbol{u^x} | \boldsymbol{u^x} = -\Lambda\boldsymbol{\delta_x}, [\boldsymbol{x}; \dot{\boldsymbol{x}}] \in \mathcal{U}_x\}. \tag{11}$$

Details of the above steady-state property will be analyzed after Lemma 1.

With this DOB structure and the designed inner-loop controller, the actual system (9) behaves similarly to the nominal system (8), which implies transient performance recovery[1]. This closed-loop property is described in Theorem 1.

Theorem 1. *Suppose that $[\boldsymbol{x}(t); \dot{\boldsymbol{x}}(t)]$ is the solution of the closed-loop actual system (9) with the designed control law (10) initiated from $[\boldsymbol{x}(0); \dot{\boldsymbol{x}}(0); \boldsymbol{y}(0); \dot{\boldsymbol{y}}(0); \boldsymbol{q}(0); \boldsymbol{p}(0)] \in \bar{\mathcal{S}}_x \times \bar{\mathcal{S}}_y \times \mathcal{S}_{qp}$ where $\mathcal{S}_{qp}$ is a known compact set of the initial values of $\boldsymbol{q}$, $\boldsymbol{p}$. For a given $\sigma \in \mathbb{R}_{++}$, there exists $\epsilon_x^* \in \mathbb{R}_{++}$ such that for each $\epsilon_x \in (0, \epsilon_x^*]$, $[\boldsymbol{x}(t); \dot{\boldsymbol{x}}(t)]$ satisfies*

$$|[\boldsymbol{x}(t); \dot{\boldsymbol{x}}(t); \boldsymbol{u}(t)] - [\bar{\boldsymbol{x}}(t); \dot{\bar{\boldsymbol{x}}}(t); \bar{\boldsymbol{u}}(t)]| \le \sigma \quad \forall t \ge 0$$

where $[\bar{\boldsymbol{x}}(0); \dot{\bar{\boldsymbol{x}}}(0); \bar{\boldsymbol{u}}(0)] = [\boldsymbol{x}(0); \dot{\boldsymbol{x}}(0); \boldsymbol{u_0}(0)]$.

Proof. Theorem 1 will be proved in the following procedure. We first rewrite the system in a standard singular perturbation form by the coordinate transformation in Lemma 1. Then, error dynamics of fast varying variables are derived, and the stability of a corresponding boundary-layer model is analyzed to obtain a reduced system. Next, inequality showing the boundedness of the transformed error variables is introduced in Lemma 2. Finally, from Lemmas 1 and 2, we prove Theorem 1 by applying Tikhonov's theorem on the infinite time interval [35], [36].

Lemma 1. *Define $\boldsymbol{\zeta} = [\boldsymbol{\zeta_1}; \boldsymbol{\zeta_2}; ...; \boldsymbol{\zeta_n}], \boldsymbol{\eta} = [\boldsymbol{\eta_1}; \boldsymbol{\eta_2}; ...; \boldsymbol{\eta_n}] \in \mathbb{R}^{2n}$ where*

$$\begin{aligned} \boldsymbol{\zeta_i} &= \begin{bmatrix} \zeta_{i,1} \\ \zeta_{i,2} \end{bmatrix} = \begin{bmatrix} \frac{1}{\epsilon_i}q_{i,1} + \frac{a_{i,1}}{a_{i,0}}q_{i,2} - \frac{1}{\epsilon_i}x_i \\ q_{i,2} - \dot{x}_i \end{bmatrix} \\ \boldsymbol{\eta_i} &= \begin{bmatrix} \eta_{i,1} \\ \eta_{i,2} \end{bmatrix} = \begin{bmatrix} p_{i,1} - \lambda_i\dot{q}_{i,2} \\ \epsilon_i(\dot{p}_{i,1} - \lambda_i\ddot{q}_{i,2}) \end{bmatrix}. \end{aligned}$$

[1]The closed-loop system consisting of the system dynamics (9) and the control law (10) is guaranteed to be uniformly bounded with respect to the nominal system.

By applying coordinate transformation from $[\boldsymbol{x};\boldsymbol{q};\boldsymbol{p}]$ *to* $[\boldsymbol{x};\boldsymbol{\zeta};\boldsymbol{\eta}]$*, the system (9) and (10) can be expressed as*

$$\begin{aligned}\ddot{\boldsymbol{x}} &= \bar{\boldsymbol{f}}_{\boldsymbol{x}} + \bar{G}_x\boldsymbol{u_0} + \Lambda^{-1}\boldsymbol{\Pi}(\boldsymbol{u^x}) + \boldsymbol{\delta_x}\\ \epsilon_i\dot{\boldsymbol{\zeta}}_{\boldsymbol{i}} &= A_{\zeta,i}\boldsymbol{\zeta_i} - \epsilon_i(\bar{f}_{x,i} + \bar{G}_{x,i}\boldsymbol{u} + \delta_{x,i})\boldsymbol{r_2}\\ \epsilon_i\dot{\boldsymbol{\eta}}_{\boldsymbol{i}} &= A_{\eta,i}\boldsymbol{\eta_i} - a_{i,0}\lambda_i(\bar{f}_{x,i} + \delta_{x,i})\boldsymbol{r_2}\end{aligned} \tag{12}$$

where $\boldsymbol{r_2} = [0;1]$ *and*

$$A_{\zeta,i} = \begin{bmatrix}-a_{i,1} & 1\\ -a_{i,0} & 0\end{bmatrix}, \quad A_{\eta,i} = \begin{bmatrix}0 & 1\\ -a_{i,0} & -a_{i,1}\end{bmatrix}.$$

Thanks to Lemma 1, the system is transformed in a standard singular perturbation form (12), and we can treat $\boldsymbol{\zeta}$, $\boldsymbol{\eta}$ as the fast varying variables. With the transformed system dynamics (12), quasi-steady-states of $\boldsymbol{\zeta}$, $\boldsymbol{\eta}$ can be obtained as

$$\boldsymbol{\zeta_i^*} = \begin{bmatrix}0\\0\end{bmatrix}, \quad \boldsymbol{\eta_i^*} = \begin{bmatrix}-\lambda_i\bar{f}_{x,i} - \lambda_i\delta_{x,i}\\ 0\end{bmatrix}$$

where $()^*$ denotes a quasi-steady-state of a fast varying variable. Here, define $\boldsymbol{\eta_{[1]}} = [\eta_{1,1};\eta_{2,1};...;\eta_{n,1}] \in \mathbb{R}^n$, then we can obtain $\boldsymbol{\eta^*_{[1]}} = -\Lambda\bar{\boldsymbol{f}}_{\boldsymbol{x}} - \Lambda\boldsymbol{\delta_x}$. From (10), $\boldsymbol{u^x} = \boldsymbol{\eta_{[1]}} + \Lambda\bar{\boldsymbol{f}}_{\boldsymbol{x}}$ satisfies, which implies that $\boldsymbol{u^x}$ is also a fast variable. Hence, the quasi-steady-state of $\boldsymbol{u^x}$ is $\boldsymbol{u^{x*}} = -\Lambda\boldsymbol{\delta_x}$, from which the definition of steady-state range (11) is obtained.

For further analysis, we define error variables $\tilde{\boldsymbol{\zeta}} = \boldsymbol{\zeta} - \boldsymbol{\zeta^*}$, $\tilde{\boldsymbol{\eta}} = \boldsymbol{\eta} - \boldsymbol{\eta^*} \in \mathbb{R}^{2n}$ and $\tilde{\boldsymbol{\eta}}_{\boldsymbol{[1]}} = \boldsymbol{\eta_{[1]}} - \boldsymbol{\eta^*_{[1]}} \in \mathbb{R}^n$. Then, we can derive error dynamics from (12) as

$$\begin{aligned}E_\otimes\dot{\tilde{\boldsymbol{\zeta}}} &= A_\zeta\tilde{\boldsymbol{\zeta}} - E_\otimes\Xi_2[\bar{\boldsymbol{f}}_{\boldsymbol{x}} + \bar{G}_x\boldsymbol{u_0} + \Lambda^{-1}\boldsymbol{\Pi}(\tilde{\boldsymbol{\eta}}_{\boldsymbol{[1]}} - \Lambda\boldsymbol{\delta_x}) + \boldsymbol{\delta_x}]\\ E_\otimes\dot{\tilde{\boldsymbol{\eta}}} &= A_\eta\tilde{\boldsymbol{\eta}} - E_\otimes\Xi_1\dot{\boldsymbol{\eta}}^*_{\boldsymbol{[1]}}\end{aligned} \tag{13}$$

where $A_\zeta = \texttt{blockdiag}\{A_{\zeta,1},...,A_{\zeta,n}\}$, $\Xi_2 = I_n \otimes [0;1]$, $A_\eta = \texttt{blockdiag}\{A_{\eta,1},...,A_{\eta,n}\}$, $\Xi_1 = I_n \otimes [1;0]$, $E_\otimes = E\otimes I_2$, and $\otimes$ denotes the Kronecker product. Then, to obtain a boundary-layer model [35], we introduce linearly transformed error variables as

$$\tilde{\boldsymbol{\zeta}}_{\boldsymbol{s}} = S_\otimes^{-1}\tilde{\boldsymbol{\zeta}}, \quad \tilde{\boldsymbol{\eta}}_{\boldsymbol{s}} = S_\otimes^{-1}\tilde{\boldsymbol{\eta}}, \quad S_\otimes = S\otimes I_2. \tag{14}$$

Note that $\tilde{\boldsymbol{\zeta}}_{\boldsymbol{s}}$, $\tilde{\boldsymbol{\eta}}_{\boldsymbol{s}}$ are not a function of ϵ_x, thus singular perturbation analysis [35] with respect to $\tilde{\boldsymbol{\zeta}}_{\boldsymbol{s}}$, $\tilde{\boldsymbol{\eta}}_{\boldsymbol{s}}$ in the following is well-defined. Using the fact that $S_\otimes^{-1}A_\zeta S_\otimes = A_\zeta$ and $S_\otimes^{-1}A_\eta S_\otimes = A_\eta$, the error dynamics of the transformed error variables can be written as

$$\begin{aligned}\epsilon_x\dot{\tilde{\boldsymbol{\zeta}}}_{\boldsymbol{s}} &= A_\zeta\tilde{\boldsymbol{\zeta}}_{\boldsymbol{s}} - \epsilon_x\Xi_2\boldsymbol{\xi}\\ \epsilon_x\dot{\tilde{\boldsymbol{\eta}}}_{\boldsymbol{s}} &= A_\eta\tilde{\boldsymbol{\eta}}_{\boldsymbol{s}} - \epsilon_x\Xi_1\dot{\boldsymbol{\eta}}^*_{\boldsymbol{[1]}}\end{aligned} \tag{15}$$

where $\boldsymbol{\xi} = \bar{\boldsymbol{f}}_{\boldsymbol{x}} + \bar{G}_x\boldsymbol{u_0} + \Lambda^{-1}\boldsymbol{\Pi}(\tilde{\boldsymbol{\eta}}_{\boldsymbol{[1]}} - \Lambda\boldsymbol{\delta_x}) + \boldsymbol{\delta_x}$. Then, the boundary-layer model of (15) can be expressed as the following linear equations:

$$\tilde{\boldsymbol{\zeta}}'_{\boldsymbol{s}} = A_\zeta\tilde{\boldsymbol{\zeta}}_{\boldsymbol{s}}, \quad \tilde{\boldsymbol{\eta}}'_{\boldsymbol{s}} = A_\eta\tilde{\boldsymbol{\eta}}_{\boldsymbol{s}} \tag{16}$$

where $()'$ denotes a derivative with respect to t/ϵ_x. Since A_ζ, A_η are Hurwitz, the exponential stability of (16) leads us to obtain a reduced system [35] or a quasi-steady-state of x from (12) as

$$\begin{aligned}\ddot{\boldsymbol{x}} &= \bar{\boldsymbol{f}}_{\boldsymbol{x}} + \bar{G}_x\boldsymbol{u_0} + \Lambda^{-1}\boldsymbol{\Pi}(\boldsymbol{u^{x*}}) + \boldsymbol{\delta_x}\\ &= \bar{\boldsymbol{f}}_{\boldsymbol{x}} + \bar{G}_x\boldsymbol{u_0} + \Lambda^{-1}\boldsymbol{u^{x*}} + \boldsymbol{\delta_x}\\ &= \bar{\boldsymbol{f}}_{\boldsymbol{x}} + \bar{G}_x\boldsymbol{u_0},\end{aligned} \tag{17}$$

which coincides with the nominal system (8).

Remark 1. *Since* $[\boldsymbol{x}(0);\dot{\boldsymbol{x}}(0)] \in \bar{\mathcal{S}}_x$ *and the vector field of (7) is bounded by Assumption 2, there exists* $T_1 \in \mathbb{R}_{++}$ *such that* $[\boldsymbol{x}(t);\dot{\boldsymbol{x}}(t)] \in \mathcal{U}_x$ *for all* $t \in [0,T_1]$*. Additionally, if the underactuated subsystem* $\boldsymbol{y}$ *exists, by Assumption 1,* $[\boldsymbol{y}(t);\dot{\boldsymbol{y}}(t)] \in \mathcal{U}_y$ *for all* $t \in [0,T_1]$*. On the other hand, since* $[\bar{\boldsymbol{x}}(0);\dot{\bar{\boldsymbol{x}}}(0)] = [\boldsymbol{x}(0);\dot{\boldsymbol{x}}(0)]$*, there exists* $T_2 \in \mathbb{R}_{++}$ *that satisfies the following statement:*

$$|[\boldsymbol{x}(t);\dot{\boldsymbol{x}}(t);\boldsymbol{u}(t)] - [\bar{\boldsymbol{x}}(t);\dot{\bar{\boldsymbol{x}}}(t);\bar{\boldsymbol{u}}(t)]| \le \frac{\sigma}{2} \quad \forall t \in [0,T_2].$$

Finally, $\bar{T}$ *is defined as* $\bar{T} = \min(T_1,T_2)$*.*

Lemma 2. *For the error variables* $\tilde{\boldsymbol{\zeta}}_{\boldsymbol{s}}$*,* $\tilde{\boldsymbol{\eta}}_{\boldsymbol{s}}$*, the following inequality holds for all* $t \in [0,\bar{T}]$*:*

$$|[\tilde{\boldsymbol{\zeta}}_{\boldsymbol{s}}(t);\tilde{\boldsymbol{\eta}}_{\boldsymbol{s}}(t)]| \le c_1e^{-c_2(t/\epsilon_x)}|[\tilde{\boldsymbol{\zeta}}_{\boldsymbol{s}}(0);\tilde{\boldsymbol{\eta}}_{\boldsymbol{s}}(0)]| + \Omega(\epsilon_x) \tag{18}$$

with some c_1*,* $c_2 \in \mathbb{R}_{++}$ *and a class-*$\mathcal{K}$ *function* Ω*.*

Proof. In (16), there exist symmetric positive definite matrices P_1, $P_2 \in \mathbb{R}^{2n\times 2n}$ satisfying $P_1A_\zeta + A_\zeta^\top P_1 = -I_{2n}$, $P_2A_\eta + A_\eta^\top P_2 = -I_{2n}$. Now, consider an overall Lyapunov candidate function $V(\tilde{\zeta}_s,\tilde{\eta}_s) = W_1 + W_2$ where $W_1 = \tilde{\zeta}_s^\top P_1\tilde{\zeta}_s$ and $W_2 = \tilde{\eta}_s^\top P_2\tilde{\eta}_s$. Using (15), the derivative of V is obtained as

$$\begin{aligned}V' &= \frac{\partial W_1}{\partial\tilde{\boldsymbol{\zeta}}_{\boldsymbol{s}}}(A_\zeta\tilde{\boldsymbol{\zeta}}_{\boldsymbol{s}} - \epsilon_x\Xi_2\boldsymbol{\xi}) + \frac{\partial W_2}{\partial\tilde{\boldsymbol{\eta}}_{\boldsymbol{s}}}(A_\eta\tilde{\boldsymbol{\eta}}_{\boldsymbol{s}} - \epsilon_x\Xi_1\dot{\boldsymbol{\eta}}^*_{\boldsymbol{[1]}})\\ &= -|\tilde{\boldsymbol{\zeta}}_{\boldsymbol{s}}|^2 - |\tilde{\boldsymbol{\eta}}_{\boldsymbol{s}}|^2 - 2\epsilon_x\tilde{\boldsymbol{\zeta}}_{\boldsymbol{s}}^\top P_1\Xi_2\boldsymbol{\xi} - 2\epsilon_x\tilde{\boldsymbol{\eta}}_{\boldsymbol{s}}^\top P_2\Xi_1\dot{\boldsymbol{\eta}}^*_{\boldsymbol{[1]}}\\ &\le -|\tilde{\boldsymbol{\zeta}}_{\boldsymbol{s}}|^2 - |\tilde{\boldsymbol{\eta}}_{\boldsymbol{s}}|^2 + \epsilon_x|\tilde{\boldsymbol{\zeta}}_{\boldsymbol{s}}|\|2P_1\||\boldsymbol{\xi}| + \epsilon_x|\tilde{\boldsymbol{\eta}}_{\boldsymbol{s}}|\|2P_2\||\dot{\boldsymbol{\eta}}^*_{\boldsymbol{[1]}}|.\end{aligned}$$

Recall that $\boldsymbol{\eta^*_{[1]}} = -\Lambda\bar{\boldsymbol{f}}_{\boldsymbol{x}} - \Lambda\boldsymbol{\delta_x}$, $|\boldsymbol{\xi}|$ and $|\dot{\boldsymbol{\eta}}^*_{\boldsymbol{[1]}}|$ are bounded in $t \in [0,\bar{T}]$ by Assumption 2 and Remark 1. Therefore, there exist some α_1, $\alpha_2 \in \mathbb{R}_{++}$, and the following inequality holds:

$$V' \le -\alpha_1V + \epsilon_x\alpha_2\sqrt{V}.$$

Finally, by the Comparison Lemma [35] and quadratic property of $V(\tilde{\zeta}_s,\tilde{\eta}_s)$, Lemma 2 is proved. □

Now, we can prove Theorem 1 using the above derivations and Lemmas. Recalling (17), the quasi-steady-state of x ideally follows the nominal system so that we can consider the nominal solution $[\bar{\boldsymbol{x}}(t);\dot{\bar{\boldsymbol{x}}}(t)]$ as a solution of the reduced system (17). From Remark 1, $|[\boldsymbol{x}(t);\dot{\boldsymbol{x}}(t);\boldsymbol{u}(t)] - [\bar{\boldsymbol{x}}(t);\dot{\bar{\boldsymbol{x}}}(t);\bar{\boldsymbol{u}}(t)]| \le \sigma/2$ is satisfied for all $t \in [0,\bar{T}]$, and from Lemma 2, $|[\tilde{\boldsymbol{\zeta}}_{\boldsymbol{s}}(\bar{T});\tilde{\boldsymbol{\eta}}_{\boldsymbol{s}}(\bar{T})]| \to 0$ as $\epsilon_x \to 0$. Therefore, Tikhonov's theorem on the infinite time interval [36] can be applied for $t > \bar{T}$, and Theorem 1 is proved. □

B. Tiltrotor Controller Design

Thanks to the derivation of the DOB formulation in section IV-A, a $\mathcal{C}^1$ nominal control law that asymptotically stabilizes the nominal system (8) and satisfies Assumption 1 can lead us to complete a robust controller design. From the nominal system (5) and (6), we design a controller guaranteeing exponential stability as follows:

$$\begin{aligned}\tan\bar{\phi}^r &= (\frac{1}{\bar{G}_u})(-\bar{f}_u + \ddot{x}_u^r - k_d\dot{e}_u - k_pe_u),\\ \bar{\boldsymbol{u}} &= \bar{G}_f^{-1}(-\bar{\boldsymbol{f}}_{\boldsymbol{f}} + \ddot{\boldsymbol{x}}_{\boldsymbol{f}}^{\boldsymbol{r}} - K_d\dot{\boldsymbol{e}}_{\boldsymbol{f}} - K_p\boldsymbol{e}_{\boldsymbol{f}})\end{aligned}$$

where k_p, $k_d \in \mathbb{R}_{++}$ and K_p, $K_d \in \mathbb{R}^{5\times5}$ are positive definite matrices. Here, $\boldsymbol{e_f} = \boldsymbol{x_f} - \boldsymbol{x_f^r}$ and $e_u = x_u - x_u^r$ are error variables of both fully actuated and underactuated subsystems (3), (4) where $()^r$ denotes reference value.

By applying the proposed DOB structure to both fully and underactuated subsystems, we can guarantee that the state of the tiltrotor is uniformly bounded with respect to the solution of nominal closed-loop dynamics using Theorem 1. Furthermore, since the nominal closed-loop error converges to the origin exponentially, the position and orientation error of the actual dynamics are uniformly ultimately bounded for both transient and steady-state regions.

V. CONTROL ALLOCATION

From the computed system input u, a control allocation law is required to compute low-level actuator inputs which are rotor thrusts and servomotor commands. Since there exist 10 actuators consisting of 8 rotors and 2 servomotors in spite of the 5-dimensional system input u, the tiltrotor is overactuated system. Thus, finding a proper solution among an infinite number of solutions for low-level actuator inputs is required to handle such redundancy.

A. Problem Definition

Before constructing an allocation law, we define a modified input $\boldsymbol{u_m} = [u_1; u_2; u_3/l_1; u_4/l_2; u_5/l_1]$ and a dimensionless ratio $r = k_f/l_1$ where l_1 and l_2 denote a half of a distance between the two rotor axes in one propeller group depicted in Fig. 2 and a half of a distance between the two propeller groups, respectively. k_f indicates the drag coefficient of propellers. Then, a mapping relation between the actuator input and the modified system input is expressed as follows:

$$\begin{aligned}\boldsymbol{u_m} &= B_8(\boldsymbol{\beta})\boldsymbol{f} \\ &= B_8(\boldsymbol{\beta^c})\boldsymbol{f} + [B_8(\boldsymbol{\beta}) - B_8(\boldsymbol{\beta^c})]\boldsymbol{f}\end{aligned} \tag{19}$$

where

$$B_8(\boldsymbol{\beta}) = \begin{bmatrix} s_1 & 0 & s_1 & 0 & s_2 & 0 & s_2 & 0 \\ c_1 & 0 & c_1 & 0 & c_2 & 0 & c_2 & 0 \\ -c_1 & rs_1 & c_1 & -rs_1 & c_2 & rs_2 & -c_2 & -rs_2 \\ -c_1 & 0 & -c_1 & 0 & c_2 & 0 & c_2 & 0 \\ s_1 & rc_1 & -s_1 & -rc_1 & -s_2 & rc_2 & s_2 & -rc_2 \end{bmatrix}$$

and $\boldsymbol{f} = [f_+^1; f_-^1; ...; f_+^4; f_-^4] \in \mathbb{R}^8$. Here, $f_+^i = f_u^i + f_l^i$ and $f_-^i = f_u^i - f_l^i$ where f_u^i, f_l^i denote generated thrust force from an upper and a lower propeller of the i^{th} coaxial propeller group (Fig. 2). Additionally, s_i, c_i, t_i denote the shorthands of $\sin(\beta_i)$, $\cos(\beta_i)$, $\tan(\beta_i)$, and $\boldsymbol{\beta^c} = [\beta_1^c; \beta_2^c] \in \mathbb{R}^2$ denotes a vector of servo angle command. We add and subtract $B_8(\boldsymbol{\beta^c})\boldsymbol{f}$ in (19) since directly controllable signal is $\boldsymbol{\beta^c}$ and not $\boldsymbol{\beta}$.

To further simply put the mapping equation, we define a vector $\boldsymbol{h} \in \mathbb{R}^6$ as follows

$$\boldsymbol{h} = A\boldsymbol{f} \tag{20}$$

where

$$A = \begin{bmatrix} \bar{A} & 0_{3\times4} \\ 0_{3\times4} & \bar{A} \end{bmatrix} \in \mathbb{R}^{6\times8}, \quad \bar{A} = \begin{bmatrix} 1 & 0 & 1 & 0 \\ 0 & 1 & 0 & -1 \\ 1 & 0 & -1 & 0 \end{bmatrix}.$$

Then, the mapping equation $\boldsymbol{u_m} = B_8(\boldsymbol{\beta^c})\boldsymbol{f}$ is divided as:

$$\begin{bmatrix} u_{m,1} \\ u_{m,2} \\ u_{m,4} \end{bmatrix} = \begin{bmatrix} s_1^c & s_2^c \\ c_1^c & c_2^c \\ -c_1^c & c_2^c \end{bmatrix} \begin{bmatrix} h_1 \\ h_4 \end{bmatrix}, \tag{21}$$

$$\begin{bmatrix} u_{m,3} \\ u_{m,5} \end{bmatrix} = \begin{bmatrix} rs_1^c & -c_1^c & rs_2^c & c_2^c \\ rc_1^c & s_1^c & rc_2^c & -s_2^c \end{bmatrix} \begin{bmatrix} h_2 \\ h_3 \\ h_5 \\ h_6 \end{bmatrix}. \tag{22}$$

Remark 2. *In (19), there exists an error term $[B_8(\boldsymbol{\beta}) - B_8(\boldsymbol{\beta^c})]\boldsymbol{f}$ caused by servomotors' delay. We treat this term as matched disturbance and incorporate it into the lumped disturbance $\boldsymbol{\Delta_f}$ defined in (3). Furthermore, it will be optimized so that overall disturbance is diminished. In the end, $\boldsymbol{u_m} = B_8(\boldsymbol{\beta^c})\boldsymbol{f}$ is considered as a mapping equation.*

Remark 3. *Unlike conventional multirotors, during APhI when the servo angles are not zero, the designed tiltrotor can additionally generate yaw directional body torque $u_{m,5}$ in (19) using rotor thrusts on top of conventional drag-based torque generation. Such additional yaw torque generation is represented in the odd elements of the fifth row of $B_8(\boldsymbol{\beta})$. In conclusion, the tiltrotor has the advantage of conducting the APhI task compared to conventional multirotor from avoiding rotor saturation point of view.*

B. Optimization-based Control Allocation Law

With the given value $\boldsymbol{u_m}$, we need to solve (20), (21) and (22) to find $\boldsymbol{f}$ and $\boldsymbol{\beta^c}$, and these provide a unique set of low-level actuator inputs. However, the above equations have an infinite number of solutions owing to redundancy and are hard to be solved due to high nonlinearity from $\boldsymbol{\beta_c}$ and trigonometrical functions. To simultaneously handle nonlinearity and redundancy, we divide the control allocation problem into two computationally tractable optimization problems in the hierarchy as illustrated in Fig. 4. We derive an analytic solution to the first optimization problem to handle nonlinearity and formulate the second problem as linear programming (LP).

We minimize energy consumption and servomotors' position error in the first optimization problem, and maximum thrust among all rotors is minimized in the second problem. One possible drawback of solving the optimization problem is heavy computation load which is particularly critical in the control allocation process running faster than other high-level motion controllers [13]. However, thanks to the proposed allocation algorithm that utilizes the analytic solution and LP formulation, we could achieve 400 Hz real-time computation during whole experiments.

The first step minimizes overall energy consumption and servomotors' position errors which cause the matched disturbance mentioned in Remark 2. We construct a nonlinear optimization problem as follows:

$$\begin{aligned} \min_{h_1,h_4,\boldsymbol{\beta^c}} \quad & h_1 + h_4 + w_s[(t_1^c - t_1)^2 + (t_2^c - t_2)^2], \\ \text{s.t.} \quad & \begin{bmatrix} u_{m.1} \\ u_{m,2} \\ u_{m,4} \end{bmatrix} = \begin{bmatrix} s_1^c & s_2^c \\ c_1^c & c_2^c \\ -c_1^c & c_2^c \end{bmatrix} \begin{bmatrix} h_1 \\ h_4 \end{bmatrix}. \end{aligned} \tag{23}$$

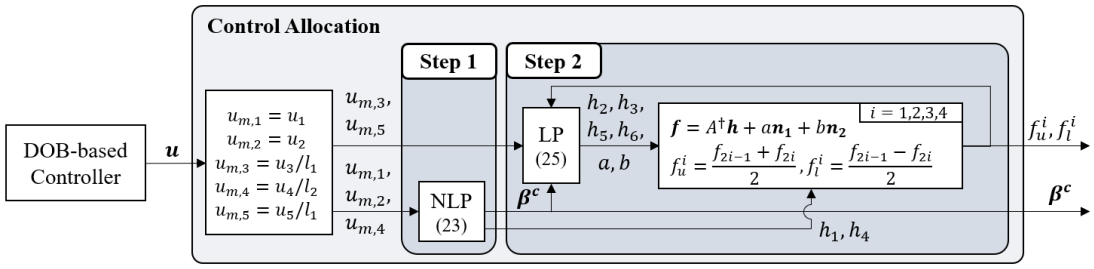

Fig. 4. Proposed optimization-based control allocator computing low-level actuator inputs. Hierarchically, step 1 resolves the nonlinearity of the mapping equation, and then constructed LP in step 2 provides the proper solution.

Since h_1+h_4 in the objective function denotes the summation of all rotor thrusts $\sum_{i=1}^{4}(f_u^i+f_l^i)$, it implies energy consumption. Also, the last term of the objective function multiplied by a weighting coefficient w_s minimizes servomotors' position errors, and the equality constraint is (21). We design such an objective function since the analytic solution can be obtained without resorting to NLP solvers which would be computationally intractable to be solved online. Assuming $s_1^c - s_2^c \simeq s_1 - s_2$ for every step, an analytic solution of (23) is obtained as follows by exploiting Karush-Kuhn-Tucker (KKT) conditions:

$$\begin{bmatrix} t_1^c \\ t_2^c \end{bmatrix} = \begin{bmatrix} \alpha_2 & -\alpha_1 \\ \alpha_1 & \alpha_2 \end{bmatrix}^{-1} \begin{bmatrix} \frac{\alpha_1\alpha_2}{w_s}(s_1 - s_2) + \alpha_2 t_1 - \alpha_1 t_2 \\ u_{m,1} \end{bmatrix}$$

where $\alpha_1 = (u_{m,2} - u_{m,4})/2$ and $\alpha_2 = (u_{m,2} + u_{m,4})/2$, and h_1, h_4 can be computed from any two rows of (21). Thus, we can treat h_1, h_4, and $\boldsymbol{\beta^c}$ as the given values for the second step optimization problem as depicted in Fig. 4.

The remaining task is to solve (20) and (22) which become linear equations thanks to the above first-step optimization problem. Here, (20) can be rewritten as follows:

$$\boldsymbol{f} = A^{\dagger}\boldsymbol{h} + a\boldsymbol{n_1} + b\boldsymbol{n_2} \tag{24}$$

where $\boldsymbol{n_1} = [0;1;0;1;0_{4\times1}]$, $\boldsymbol{n_2} = [0_{4\times1};0;1;0;1] \in \mathbb{R}^8$ denote the basis of $Null(A)$, and $a, b \in \mathbb{R}$. To effectively handle the redundancy and to provide a nonnegative solution, we construct LP for the second step optimization problem as follows:

$$\begin{aligned} \min_{\substack{h_j,a,b,s,\\ \mu_{i,u},\mu_{i,l}}} \quad & s + w_\mu(\mu_{1,u} + \mu_{1,l} + \ldots + \mu_{4,u} + \mu_{4,l}), \\ \text{s.t.} \quad & \begin{bmatrix} u_{m,3} \\ u_{m,5} \end{bmatrix} = \begin{bmatrix} rs_1^c & -c_1^c & rs_2^c & c_2^c \\ rc_1^c & s_1^c & rc_2^c & -s_2^c \end{bmatrix} \begin{bmatrix} h_2 \\ h_3 \\ h_5 \\ h_6 \end{bmatrix}, \\ & |f_{u,pre}^i - f_u^i| \le \mu_{i,u}, \quad |f_{l,pre}^i - f_l^i| \le \mu_{i,l}, \\ & 0 \le f_u^i \le s, \quad 0 \le f_l^i \le s, \quad i = 1,2,3,4 \end{aligned} \tag{25}$$

where $f_{u,pre}^i$ and $f_{l,pre}^i$ denote the values of f_u^i and f_l^i computed in the previous time step. Also, although inequality constraints are written using f_u^i, f_l^i for convenience, these are linear inequalities with respect to $\boldsymbol{h}$, a, b, referring to (24). For the proposed objective function, s minimizes the maximum thrust among all rotors to avoid rotor saturation. The μ variables with a weighting coefficient w_μ are additionally introduced to prevent large oscillation of rotor thrust which highly affects the control performance.

Note that one can thoroughly minimize the effect of rotor saturation by setting the weighting factor w_μ zero; however, we observe in actual experiments that setting nonzero w_μ is crucial in mitigating thrust oscillation. Consequently, with the proposed allocation law based on the hierarchical optimization problem (23) and (25), we obtain low-level inputs consisting of 8 rotors' thrusts and 2 servomotors' commands.

Remark 4. *The effort to minimize $\boldsymbol{\beta} - \boldsymbol{\beta^c}$ contributes to reducing the magnitude of the lumped disturbance $\boldsymbol{\Delta_f}$ in (3) in two aspects. First, the magnitude of the error term caused by the servomotors' delay $[B_8(\boldsymbol{\beta}) - B_8(\boldsymbol{\beta^c})]\boldsymbol{f}$ appeared in Remark 2 can be directly mitigated. Furthermore, the effort may contribute to inducing smaller acceleration $\ddot{\boldsymbol{\beta}}$ and velocity $\dot{\boldsymbol{\beta}}$ of servomotors which compose the lumped disturbance $\boldsymbol{\Delta_f}$ referring (2) and (3).*

Remark 5. *Setting $a = b = 0$ in (24) and similarly applying pseudo-inverse to (22), which we call a naive pseudo-inverse method, we can easily obtain $\boldsymbol{f}$. However, such pseudo-inverse method neither consider the nonnegativity of computed thrusts nor exploit redundancy advantageously; thus, rotor saturation avoidance cannot be directly considered. The effectiveness of the proposed LP in preventing rotor saturation compared to the naive pseudo-inverse method is validated in experiments.*

Remark 6. *A rotor saturation-related hard constraint can be imposed as $s \le f_{max}$ where f_{max} is the maximum available rotor thrust. However, considering (25) with $w_\mu = 0$, saturation avoidance is still available without such hard constraint which may rather incur infeasibility. Firstly, if there exists at least one solution satisfying the condition $s \le f_{max}$, then the formulated LP (25) with $w_\mu = 0$ finds a solution with saturation avoidance property by definition. Secondly, even when there exists no solution satisfying the hard constraint (e.g. when an excessively large high-level control input is provided), the LP does not encounter infeasibility. This property of the proposed LP could provide control recovery after excessively large control command disappears, possibly preventing the worst crashing scenario.*

VI. RESULTS

In this section, we present real-world experiments validating the proposed overall framework for heavy object pushing task

using the designed tiltrotor. Before conducting main experiments, preliminary experiments that validate the effectiveness of each proposed controller and allocation algorithm will be introduced. For the first main scenario, we conduct an interaction force measuring experiment to show the tiltrotor's capability of stably generating large horizontal force without rotor saturation. Next, we repeatedly conduct heavy object pushing experiments with varying weights of the object. All experiments are successful even without any knowledge of the weight of the object and interaction model, which validates the robustness of the proposed controller and allocation law. In experiments mentioned above, as stated in Remark 5, we compare the proposed control allocation algorithm with a naive pseudo-inverse method to demonstrate the effectiveness of the proposed control allocation law in avoiding rotor saturation. We execute both algorithms of the proposed and naive pseudo-inverse methods during Experiments 1–3, but only the signal computed from the proposed method is transmitted to actuators. Lastly, we provide a comparative experiment using a conventional multirotor which has the same physical property as the tiltrotor for fair comparison. This manifests validity of the designed tiltrotor in achieving heavy object pushing task.[2]

A. Experimental Setup

A customized 5-CDoF coaxial tiltrotor is constructed as described in Fig. 2. Details of used components and physical properties of the tiltrotor are shown in Table I. Here, although only two servomotors are required for the tilting mechanism of rotors, one additional servomotor is used to install a 1-DoF robotic arm with an end-effector. This is only to compensate the pitch angle during comparative experiments using a conventional multirotor which requires a nonzero pitch angle to generate a horizontal interaction force. All experiments are performed under the Optitrack motion capture system providing a pose measurement to an onboard computer at 100 Hz. Together with IMU measurements, the full state of the tiltrotor is estimated using an error state Kalman filter whose implementation details can be found in [37]. Before the main experiments, we conduct a pre-experiment to obtain a mapping between the PWM signal and thrust using Tyto series 1585 thrust stand with RCbenchmark data-acquisition software. In addition, from this pre-experiment, we can obtain the drag coefficient k_f of the used propeller which indicates drag-based torque to thrust force ratio.

Design parameters of the DOB-based controller and control allocation can be found in Table II. Here, subscripts f and u indicate DOB parameters of fully actuated and underactuated subsystems, respectively. We set $a_{i,0}$, $a_{i,1}$ in (10) as constant for all i, whose values are listed in Table II. Note that Λ_f in the Table is obtained from $\Lambda_f = \texttt{blockdiag}\{\sqrt{m}I_2, J^{1/2}\}$. In implementing the proposed control allocation algorithm, we solve LP in (25) using a commercial off-the-shelf CPLEX LP solver [38] running at 400 Hz. All the algorithms are executed on an onboard computer Intel NUC using Robot Operating System (ROS) in Ubuntu 20.04.

[2]An experimental video can be found at https://youtu.be/Gdmcmoz_UjU

TABLE I
MAIN COMPONENTS OF THE SYSTEM AND PHYSICAL PROPERTIES (DIAGONAL ELEMENTS FOR MATRIX)

Component	Product name	Quantity
Onboard computer	Intel NUC i7	1
Rotor	KDE2315XF-965	8
Propeller	APC B9x4.5MR-B4	8
Servomotor	Dynamixel XM430 series	3
ESC	Hobbywing XRotor Micro 40A 4in1	2
PWM generator	Nucleo F446RE	1
IMU sensor	Vectornav VN-100	1
Battery (computer)	Turnigy 2,200 mAh 4S LiPo	1
Battery (actuators)	Turnigy 4,200 mAh 6S LiPo	1
Parameter	**Value**	**Units**
m	3.3	kg
J	$(0.025, 0.035, 0.045)$	kgm^2
l_1, l_2	0.17, 0.15	m
k_f	0.016	Nm/N

TABLE II
CONTROLLER AND CONTROL ALLOCATION PARAMETERS (DIAGONAL ELEMENTS FOR MATRICES)

Controller			
Parameter	Value	Parameter	Value
Λ_f	$(1.82, 1.82, 0.158, 0.187, 0.212)$	Λ_u	1.0
E_f	$(0.3, 0.5, 0.1, 1.0, 0.5)$	E_u	1.0
K_p	$(6.0, 6.0, 90.0, 120.0, 15.0)$	k_p	6.0
K_d	$(4.0, 4.0, 30.0, 30.0, 15.0)$	k_d	4.5
a_0	1.0	a_1	2.0
Allocation			
Parameter	Value	Parameter	Value
w_s	600.0	w_μ	1.0

B. Planning for Object Pushing

A planning process for reference generation is required to conduct experiments using autonomous robots. In this regard, several planning techniques considering various constraints such as collision avoidance [39], [40] could be employed. However, to concentrate on demonstrating the contribution of this work separately, we only focus on push planning.

To enable object pushing, an unknown but sufficiently large interaction force should be applied to the object. To induce such interaction force while utilizing the proposed robust controller, we adopt a simple but effective strategy for setpoint planning: assigning a *penetrating* setpoint behind the contact surface of the object. Thanks to the disturbance rejection property of the proposed DOB-based robust controller, even without modulating the setpoint to further deviate from the contact surface of the object, interaction force will accumulate, eventually leading to the sufficient magnitude to push the object. Thanks to this observation, a setpoint planner no longer needs to additionally update the setpoint in the penetrating direction as previously done in [7]. After the object moves, we modify the setpoint to be on the contact surface of the object to prevent excessive position error accumulation.

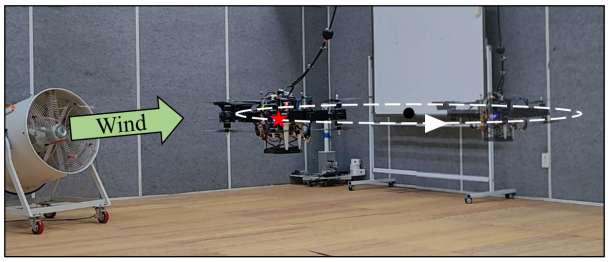

Fig. 5. Composite image of preliminary experiment related to controller validation – circular trajectory tracking under the wind disturbance.

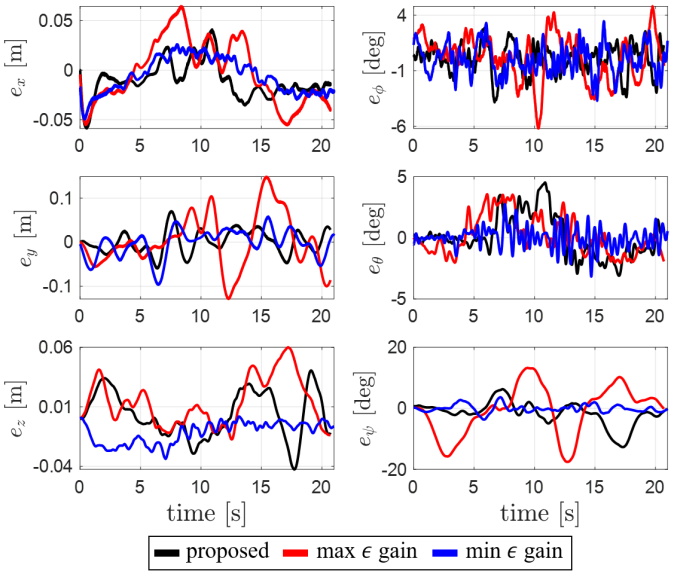

Fig. 6. Results for preliminary experiment related to controller validation (Fig. 5). Maximum and minimum ϵ are chosen as 0.1 and 1.0 referring to the tuned multivariable gain E_f in Table II.

C. Preliminary experiments – controller & control allocation validation

We conduct preliminary experiments to validate the individual effectiveness of 1) proposed DOB-based controller and 2) control allocation law. First, to validate effectiveness of the proposed multivariable control gain formulation in the DOB-based controller, we compare the proposed method with other approaches where a constant ϵ gain is selected. We perform circular trajectory tracking experiments as shown in Fig. 5. To elaborate, the tracking experiments are repeatedly conducted with the presence of time-varying wind disturbance (maximum 3 $\mathrm{m/s}$). Here, according to Theorem 1, using the smaller values of ϵ theoretically ensures that the nominal and actual systems behave similarly. For comparison, the constant ϵ values are chosen as 0.1 and 1.0 which are the minimum and maximum values of the tuned multivariable gain E_f in Table II. Position and orientation errors are plotted in Fig. 6 where *proposed* denotes the tuned multivariable ϵ gain. Here, consistent with theoretical analysis, we observe that smaller values of ϵ tend to decrease the error bound. On the other hand, although the result of the minimum ϵ shows the smallest error bound, there exists perceptible vibration especially in roll and pitch angles. This is due to practical issues such as measurement noise. The oscillation of the fuselage could critically affect overall stability in situations with larger disturbances such as pushing a heavy object. Therefore, thanks to the proposed DOB reformulation that enables the use of multivariable ϵ, we can effectively use smaller values of ϵ in the desired states or directions as much as possible and increase ϵ in directions where oscillations are severe.

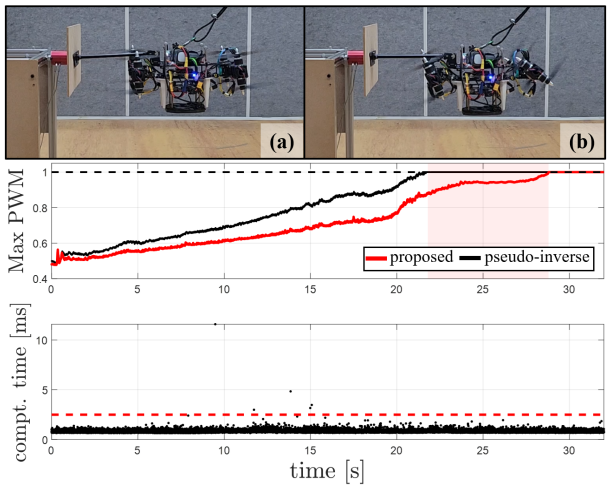

Fig. 7. Image of preliminary experiment related to validation of control allocation (upper) – (a) start to push static environment, (b) pushing static environment. Results for the experiment (lower). Red colored patch (22 s $\sim$ 29 s) emphasizes the effectiveness of the proposed control allocation algorithm in avoiding rotor saturation compared to the pseudo-inverse method.

Next, for comprehensive validation regarding the proposed control allocation algorithm, we conduct an experiment using the pseudo-inverse method (Remark 5) while simultaneously comparing the computation result of the proposed allocation algorithm. To elaborate the scenario, the tiltrotor pushes a static environment using the pseudo-inverse method until it becomes unstable. At the same time, rotor PWM values computed from the proposed allocation algorithm are recorded, and the maximum among the PWM signals are plotted as in Fig. 7. Here, it can be observed that the rotor saturation is effectively avoided for about 7 s. Also, as shown in Fig. 7, the result displaying computation time confirms the real-time applicability of the proposed optimization-based allocation algorithm which is running at 400 Hz. Through this experiment, we validate the superiority of the proposed method and rationalize that the main experiments are performed using the proposed control allocation algorithm.

D. Experiment 1 – Capability of the tiltrotor in horizontal force generation

We conduct the experiment of measuring the interaction force while pushing against a wall whose result is in Fig. 8. Here, we exploit the FUTEK MBA500 load cell to measure the force. As displayed in the upper plot of Fig. 8, the experiment includes not only a pushing process of generating gradually increasing horizontal force f_x, but also a process of recovering to an initial hovering state. This ensures that the aerial robot can maintain stability during the force generation.

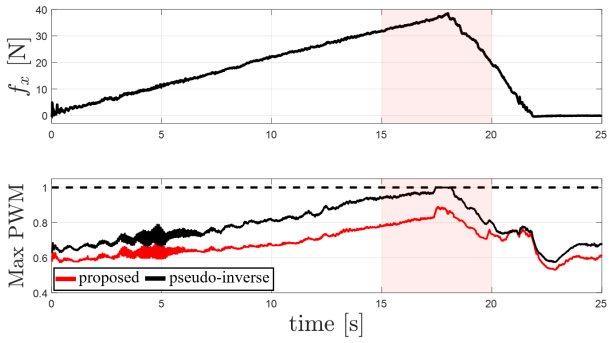

Fig. 8. Results for experiment 1 validating capability of the tiltrotor. Red colored patch (15 s $\sim$ 20 s) emphasizes the effectiveness of the proposed control allocation law in preventing rotor saturation when the tiltrotor is generating a relatively large interaction force.

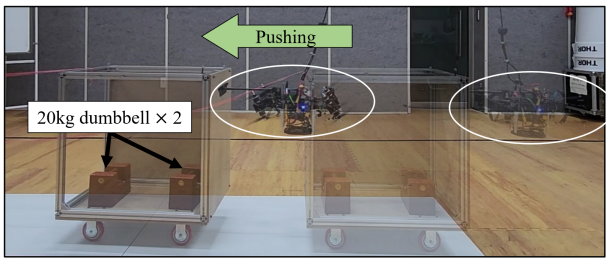

Fig. 9. Composite image of experiment 2 – pushing a cart loaded with two 20 kg dumbbells (overall 60 kg).

An oscillation of PWM signals in the lower plot of Fig. 8 around 5 s is observed, which shows the stabilizing effort of the tiltrotor against inevitable time-varying disturbance. The above phenomenon can be frequently observed when a hovering aerial robot begins to interact with an environment. According to the upper plot in Fig. 8, the tiltrotor succeeds in generating about 40 N of a horizontal interaction force that is greater than 1.2 times the weight of the tiltrotor. Such a result validates the capability of generating a large interaction force stably. The bottom plot showing maximum PWM signals suggests that the tiltrotor can even generate a larger force thanks to the remaining thrust margin. Furthermore, as can be found in the red-shaded time range in Fig. 8, the proposed allocation law effectively prevents rotor saturation unlike the naive pseudo-inverse method (Remark 5).

E. Experiment 2 – Heavy object pushing

We conduct cart-pushing experiments to validate the proposed strategy for heavy object pushing task (Fig. 9). To demonstrate the robustness of the proposed strategy in various environment settings, we perform three different cart-pushing experiments where we vary the weight of the cart using additional weights. Experimental results with a 20 kg cart additionally equipped with 20 kg and 40 kg dumbbells are provided in Figs. 10 and 11 where the result with an empty cart is displayed in the attached video. In Figs. 10 and 11, for the upper three plots, solid lines and dotted lines denote measurement data and their reference or command values, respectively. Especially for the top plot of each figure, x_e and y_e denote the horizontal position of an end-effector of

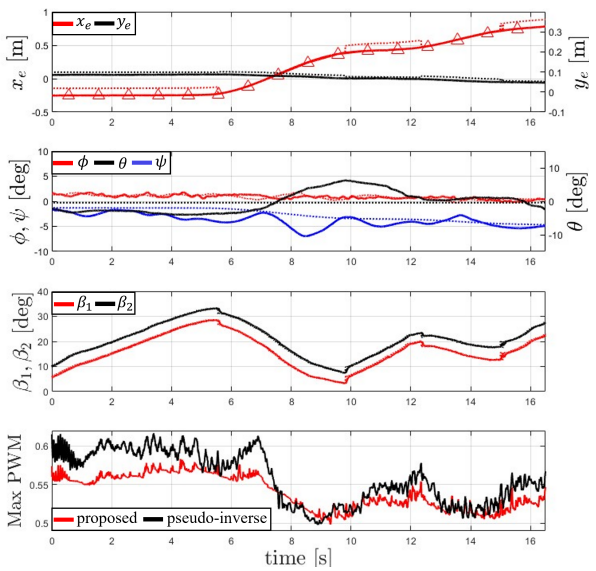

Fig. 10. Results for experiment 2 – pushing a cart equipped with 20 kg additional weight (overall 40 kg).

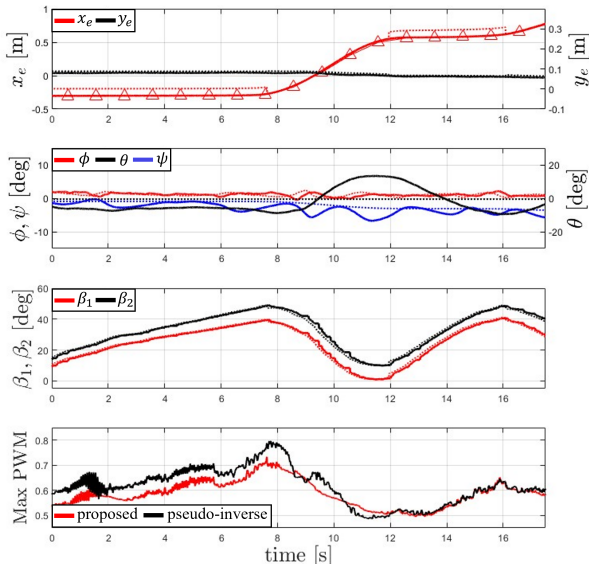

Fig. 11. Results for experiment 2 – pushing a cart equipped with 40 kg additional weight (overall 60 kg).

the tiltrotor while triangle markers denote the x-coordinate of the cart's interacting point in O_w. Also, the remaining plots display trajectories of Euler angles (ϕ, θ, ψ) of the tiltrotor and tilt angles (β_1, β_2) of servomotors, and time history of the maximum PWM signal among all 8 rotors is plotted at the bottom.

Figs. 10 and 11 show that the proposed strategy with the designed tiltrotor successfully achieves the object pushing task without any knowledge of the object's physical properties and frictional model. As can be found in the plots, the error of roll and yaw angles are bounded within 5 deg throughout the whole experiments, which confirms stability and transient performance recovery. The same is also true for the pitch angle, but a slightly larger deviation occurs in Fig. 11. This

is because, while pushing the heaviest cart of 60 kg, an inevitable disturbance including reaction torques incurred from servomotors is exerted predominantly to the pitch direction. The large servomotor torques are induced from a sudden descent in the servo angle command $\boldsymbol{\beta}^{\boldsymbol{c}}$, and this is again mainly caused by a sudden drop in interaction force after the cart is pushed. Since this servomotor torque is not measurable nor directly controllable in most aerial robot applications due to the use of lightweight servomotors, such torque can only be addressed as a disturbance. Even in the presence of such disturbance, we could observe uniform boundedness of all states thanks to the proposed robust controller for rejecting disturbance and control allocation law for reducing the servo angle position error.

Lastly, the maximum PWM signal among 8 PWM signals transmitted to the rotors at every instant is plotted in the bottom of Figs. 10 and 11. Comparison is made with the naive pseudo-inverse method that appeared in Remark 5. In all the experiments, the proposed allocation law outperforms the pseudo-inverse method in most time intervals where the proposed method shows a lower maximum PWM value than the compared method. We presume that few occurrences of the opposite situation are owing to the soft constraint imposed on the proposed optimization problem (25) which minimizes deviation between the desired thrust and the current thrust. Such behavior will be eliminated if we set the weight related to such soft constraint as zero $w_\mu = 0$. However, we also observe that such undesirable opposite situation only occurs during recovery after the object is pushed, for example, the time interval between $t = 7$ s and $t = 9$ s in Fig. 10 and that between $t = 10$ s and $t = 12$ s in Fig. 11. Since rotor saturation is usually not an issue during recovery, we can assure that the proposed method provides sufficient rotor saturation avoidance when it matters.

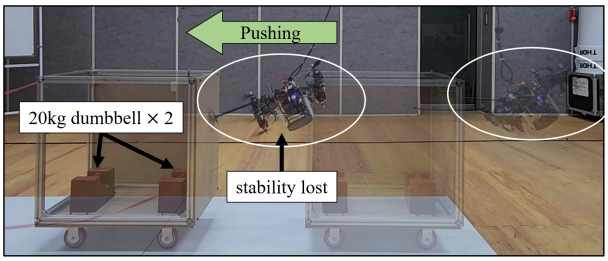

Fig. 12. Composite image of experiment 3 – comparative study with a conventional multirotor. During the experiment, the aerial robot loses stability due to rotor saturation, and we manually pull the safety rope attached above the aerial robot to prevent a crash.

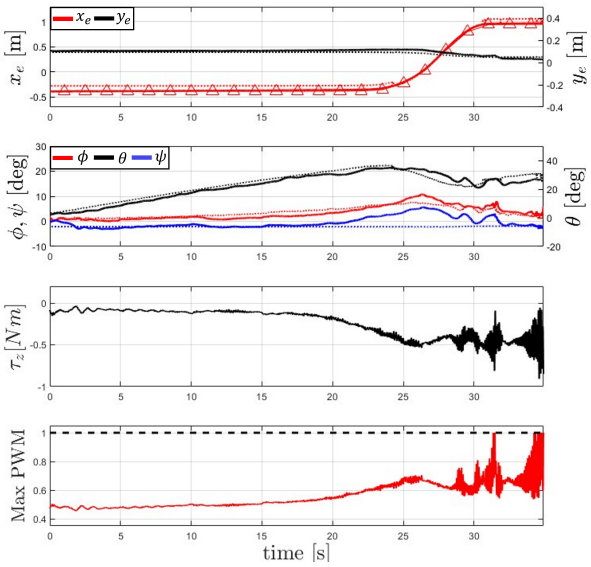

Fig. 13. Results for experiment 3 – comparative experiment using a conventional multirotor. The same coaxial tiltrotor platform is employed but with fixed zero tilt angles.

F. Experiment 3 – Comparative study using a conventional multirotor

To validate the effectiveness of the considered tiltrotor hardware, we conduct a comparative study with a conventional multirotor. For a fair comparison, we use the same coaxial tiltrotor hardware but with fixed zero tilt angles. In Fig. 13, for the upper two plots displaying the pose history of the tiltrotor, solid and dotted lines respectively denote measurement and reference data as in the case of experiment 2. Here, for the plot in the third row, τ_z indicates the yaw directional body torque computed by the DOB-based controller designed for a 4-CDoF conventional multirotor [7].

Although only displayed in the attached video, the conventional multirotor achieves to push an empty 20 kg cart and a cart loaded with a single 20 kg dumbbell. However, when pushing a cart loaded with two 20 kg dumbbells, whose environment setting is equivalent to the heaviest case of experiment 2, the multirotor fails. Among the two trials in the same setting, Fig. 13 illustrates the only case that includes a movement of the cart while the other case fails even in an initial push and loses stability. The experimental result in Figs. 12, 13 shows that the conventional multirotor eventually becomes unstable although the multirotor initially pushes the heavy cart. As depicted in the bottom of Fig. 13 showing the maximum PWM signal, it is evident that the rotor becomes saturated during the experiment. This saturation ultimately leads to failure. As shown in the third and bottom plots of Fig. 13, the tendency of oscillation in both the body yaw torque τ_z and the maximum PWM value among 8 rotors appears to be similar and highly correlated, implying that τ_z may play a significant role in rotor saturation causing the loss of stability. Through this comparative study, we validate the necessity of the proposed framework by showing that it is challenging to achieve heavy object pushing using conventional multirotors due to rotor saturation.

VII. CONCLUSIONS

This paper presented an overall framework for performing a heavy object pushing task using a tiltrotor. The main challenges are to maintain stability in the presence of uncertain motion of the interacting object and to prevent rotor saturation while generating a sufficiently large interaction force to push a heavy object. To address these challenges, we proposed a strategy composed of a robust controller design and control

allocation algorithm. We designed the H-shaped coaxial tiltrotor suitable for heavy object pushing by effectively utilizing rotor thrusts in generating both horizontal interaction force and yaw torque. Next, by introducing a robust controller based on the nonlinear DOB, we ensured both transient and steady-state performance even in the presence of unknown motion of the interacting object. Lastly, we prevented rotor saturation by exploiting redundancy in the control allocation problem. A hierarchy of optimization problems was formulated to address hardware-inherent nonlinearity, and we derived an analytic solution to the first problem and designed the second problem as LP to facilitate real-time computation. Applicability of the overall framework was validated in the real-world experiments.

REFERENCES

[1] D. Lee, H. Seo, D. Kim, and H. J. Kim, "Aerial manipulation using model predictive control for opening a hinged door," in *2020 IEEE Int. Conf. Robot. Autom.* IEEE, 2020, pp. 1237–1242.

[2] N. Sugito, M. Zhao, T. Anzai, T. Nishio, K. Okada, and M. Inaba, "Aerial manipulation using contact with the environment by thrust vectorable multilinked aerial robot," in *2022 IEEE Int. Conf. Robot. Autom.* IEEE, 2022, pp. 54–60.

[3] M. Brunner, L. Giacomini, R. Siegwart, and M. Tognon, "Energy tank-based policies for robust aerial physical interaction with moving objects," in *2022 IEEE Int. Conf. Robot. Autom.* IEEE, 2022, pp. 2054–2060.

[4] F. Benzi, M. Brunner, M. Tognon, C. Secchi, and R. Siegwart, "Adaptive tank-based control for aerial physical interaction with uncertain dynamic environments using energy-task estimation," *IEEE Robot. Autom. Lett.*, vol. 7, no. 4, pp. 9129–9136, 2022.

[5] K. Galloway, K. Sreenath, A. D. Ames, and J. W. Grizzle, "Torque saturation in bipedal robotic walking through control lyapunov function-based quadratic programs," *IEEE Access*, vol. 3, pp. 323–332, 2015.

[6] S. Kim, S. Choi, H. Kim, J. Shin, H. Shim, and H. J. Kim, "Robust control of an equipment-added multirotor using disturbance observer," *IEEE Trans. Control Syst. Technol.*, vol. 26, no. 4, pp. 1524–1531, 2017.

[7] D. Lee, H. Seo, I. Jang, S. J. Lee, and H. J. Kim, "Aerial manipulator pushing a movable structure using a dob-based robust controller," *IEEE Robot. Autom. Lett.*, vol. 6, no. 2, pp. 723–730, 2021.

[8] J. Byun, D. Lee, H. Seo, I. Jang, J. Choi, and H. J. Kim, "Stability and robustness analysis of plug-pulling using an aerial manipulator," in *2021 IEEE Int. Conf. Intell. Robots Syst.* IEEE, 2021, pp. 4199–4206.

[9] J. Liang, Y. Chen, N. Lai, B. He, Z. Miao, and Y. Wang, "Low-complexity prescribed performance control for unmanned aerial manipulator robot system under model uncertainty and unknown disturbances," *IEEE Transactions on Industrial Informatics*, vol. 18, no. 7, pp. 4632–4641, 2021.

[10] C. Ding and L. Lu, "A tilting-rotor unmanned aerial vehicle for enhanced aerial locomotion and manipulation capabilities: Design, control, and applications," *IEEE ASME Trans. Mechatron.*, vol. 26, no. 4, pp. 2237–2248, 2021.

[11] R. B. Anderson, J. A. Marshall, and A. L'Afflitto, "Constrained robust model reference adaptive control of a tilt-rotor quadcopter pulling an unmodeled cart," *IEEE Transactions on Aerospace and Electronic Systems*, vol. 57, no. 1, pp. 39–54, 2021.

[12] R. Watson, M. Kamel, D. Zhang, G. Dobie, C. MacLeod, S. G. Pierce, and J. Nieto, "Dry coupled ultrasonic non-destructive evaluation using an over-actuated unmanned aerial vehicle," *IEEE Trans. Autom. Sci. Eng.*, vol. 19, no. 4, pp. 2874–2889, 2022.

[13] M. Kamel, S. Verling, O. Elkhatib, C. Sprecher, P. Wulkop, Z. Taylor, R. Siegwart, and I. Gilitschenski, "The voliro omniorientational hexacopter: An agile and maneuverable tiltable-rotor aerial vehicle," *IEEE Robot. Autom. Mag.*, vol. 25, no. 4, pp. 34–44, 2018.

[14] M. Allenspach, K. Bodie, M. Brunner, L. Rinsoz, Z. Taylor, M. Kamel, R. Siegwart, and J. Nieto, "Design and optimal control of a tiltrotor micro-aerial vehicle for efficient omnidirectional flight," *Int. J. Rob. Res.*, vol. 39, no. 10-11, pp. 1305–1325, 2020.

[15] H. Li, X. Zheng, H. He, and L. Liao, "Design and longitudinal dynamics decoupling control of a tilt-rotor aerial vehicle with high maneuverability and efficiency," *IEEE Robot. Autom. Lett.*, 2023.

[16] Z.-Y. Lv, Y. Wu, Q. Zhao, and X.-M. Sun, "Design and control of a novel coaxial tilt-rotor uav," *IEEE Trans. Ind. Electron.*, vol. 69, no. 4, pp. 3810–3821, 2021.

[17] M. Ryll, H. H. Bülthoff, and P. R. Giordano, "A novel overactuated quadrotor unmanned aerial vehicle: Modeling, control, and experimental validation," *IEEE Trans. Control Syst. Technol.*, vol. 23, no. 2, pp. 540–556, 2015.

[18] P. Yu, Y. Su, M. J. Gerber, L. Ruan, and T.-C. Tsao, "An over-actuated multi-rotor aerial vehicle with unconstrained attitude angles and high thrust efficiencies," *IEEE Robot. Autom. Lett.*, vol. 6, no. 4, pp. 6828–6835, 2021.

[19] S. Wang, L. Ma, B. Li, and K. Zhang, "Architecture design and flight control of a novel octopus shaped multirotor vehicle," *IEEE Robot. Autom. Lett.*, vol. 7, no. 1, pp. 311–317, 2022.

[20] Y. Su, P. Yu, M. J. Gerber, L. Ruan, and T.-C. Tsao, "Nullspace-based control allocation of overactuated uav platforms," *IEEE Robot. Autom. Lett.*, vol. 6, no. 4, pp. 8094–8101, 2021.

[21] Y. Su, C. Chu, M. Wang, J. Li, L. Yang, Y. Zhu, and H. Liu, "Downwash-aware control allocation for over-actuated uav platforms," in *2022 IEEE Int. Conf. Intell. Robots Syst.* IEEE, 2022, pp. 10 478–10 485.

[22] Y. Su, L. Ruan, P. Yu, C.-H. Pi, M. J. Gerber, and T.-C. Tsao, "A fast and efficient attitude control algorithm of a tilt-rotor aerial platform using inputs redundancies," *IEEE Robotics and Automation Letters*, vol. 7, no. 2, pp. 1214–1221, 2022.

[23] J. A. Bezerra and D. A. Santos, "Optimal exact control allocation for under-actuated multirotor aerial vehicles," *IEEE Control Systems Letters*, vol. 6, pp. 1448–1453, 2022.

[24] D. Brescianini and R. D'Andrea, "Computationally efficient trajectory generation for fully actuated multirotor vehicles," *IEEE Trans. Robot.*, vol. 34, no. 3, pp. 555–571, 2018.

[25] M. Ryll, G. Muscio, F. Pierri, E. Cataldi, G. Antonelli, F. Caccavale, D. Bicego, and A. Franchi, "6d interaction control with aerial robots: The flying end-effector paradigm," *Int. J. Rob. Res.*, vol. 38, no. 9, pp. 1045–1062, 2019.

[26] R. B. Anderson, J. A. Marshall, A. L'Afflitto, and J. M. Dotterweich, "Model reference adaptive control of switched dynamical systems with applications to aerial robotics," *Journal of Intelligent & Robotic Systems*, vol. 100, pp. 1265–1281, 2020.

[27] K. Bodie, M. Brunner, M. Pantic, S. Walser, P. Pfändler, U. Angst, R. Siegwart, and J. Nieto, "Active interaction force control for contact-based inspection with a fully actuated aerial vehicle," *IEEE Trans. Robot.*, vol. 37, no. 3, pp. 709–722, 2021.

[28] H. Lee, B. Yu, C. Tirtawardhana, C. Kim, M. Jeong, S. Hu, and H. Myung, "Caros-q: Climbing aerial robot system adopting rotor offset with a quasi-decoupling controller," *IEEE Robot. Autom. Lett.*, vol. 6, no. 4, pp. 8490–8497, 2021.

[29] C. Ding, L. Lu, C. Wang, and C. Ding, "Design, sensing, and control of a novel uav platform for aerial drilling and screwing," *IEEE Robot. Autom. Lett.*, vol. 6, no. 2, pp. 3176–3183, 2021.

[30] C. Papachristos, K. Alexis, and A. Tzes, "Efficient force exertion for aerial robotic manipulation: Exploiting the thrust-vectoring authority of a tri-tiltrotor uav," in *2014 IEEE international conference on robotics and automation (ICRA)*. IEEE, 2014, pp. 4500–4505.

[31] J. Tang, K. P. Jain, and M. W. Mueller, "Quartm: A quadcopter with unactuated rotor tilting mechanism capable of faster, more agile, and more efficient flight," *Frontiers in Robotics and AI*, vol. 9, p. 1033715, 2022.

[32] P. Zheng, X. Tan, B. B. Kocer, E. Yang, and M. Kovac, "Tiltdrone: A fully-actuated tilting quadrotor platform," *IEEE Robot. Autom. Lett.*, vol. 5, no. 4, pp. 6845–6852, 2020.

[33] S. Kim, S. Choi, and H. J. Kim, "Aerial manipulation using a quadrotor with a two dof robotic arm," in *2013 IEEE Int. Conf. Intell. Robots Syst.* IEEE, 2013, pp. 4990–4995.

[34] J. Back and H. Shim, "An inner-loop controller guaranteeing robust transient performance for uncertain mimo nonlinear systems," *IEEE Trans. Automat. Contr.*, vol. 54, no. 7, pp. 1601–1607, 2009.

[35] H. K. Khalil and J. W. Grizzle, *Nonlinear systems*. Prentice hall Upper Saddle River, NJ, 2002, vol. 3.

[36] F. C. Hoppensteadt, "Singular perturbations on the infinite interval," *Trans. Am. Math. Soc.*, vol. 123, no. 2, pp. 521–535, 1966.

[37] [Online]. Available: https://github.com/ChanghyeonKim93/error_state_kalman_filter_ros

[38] I. CPLEX, "22.1.0 user's manual," 2022.

[39] S. Liu, M. Watterson, K. Mohta, K. Sun, S. Bhattacharya, C. J. Taylor, and V. Kumar, "Planning dynamically feasible trajectories for quadrotors using safe flight corridors in 3-d complex environments," *IEEE Robotics and Automation Letters*, vol. 2, no. 3, pp. 1688–1695, 2017.

[40] X. Wang, Z. Deng, H. Peng, L. Wang, Y. Wang, L. Tao, C. Lu, and Z. Peng, "Autonomous docking trajectory optimization for unmanned

surface vehicle: A hierarchical method," *Ocean Engineering*, vol. 279, p. 114156, 2023.

Sunwoo Hwang (Graduate Student Member, IEEE) received the B.S. degree in mechanical engineering in 2022 from Seoul National University, Seoul, South Korea, where he is currently working toward an integrated M.S./Ph.D. degree in aerospace engineering.

His current research interests include control and planning of robotic systems.

Dongjae Lee (Graduate Student Member, IEEE) received the B.S. and M.S. degrees in mechanical and aerospace engineering in 2018 and 2020, respectively, from Seoul National University, Seoul, South Korea, where he is currently working toward the Ph.D. degree in aerospace engineering.

His current research interests include control and planning of robotic systems.

Changhyeon Kim (Member, IEEE) received the B.S., M.S. and Ph.D. degrees from the Department of Mechanical and Aerospace Engineering, Seoul National University, Seoul, South Korea, in 2016, 2018 and 2023, respectively.

He is currently a researcher with Samsung Research, Seoul, South Korea. His current research interests include 3-D reconstruction, visual navigation and camera–IMU–LiDAR fusion.

Hyoun Jin Kim (S'98-M'02) received the B.S. degree from the Korea Advanced Institude of Technology, Daejeon, South Korea, in 1995, and the M.S. and Ph.D. degrees in mechanical engineering from the University of California at Berkeley (UC Berkeley), Berkeley, CA, USA, in 1999 and 2001, respectively.

From 2002 to 2004, she was a Post-Doctoral Researcher in electrical engineering and computer science with UC Berkeley. In 2004, she joined the Department of Mechanical and Aerospace Engineering, Seoul National University, Seoul, South Korea, as an Assistant Professor, where she is currently a Professor. Her current research interests include intelligent control of robotic systems and motion planning.